

NASA
Technical
Paper
3385

November 1993

1N-02
198097
59P

Internal Performance of a Nonaxisymmetric Nozzle With a Rotating Upper Flap and a Center-Pivoted Lower Flap

David J. Wing,
Laurence D. Leavitt,
and Richard J. Re

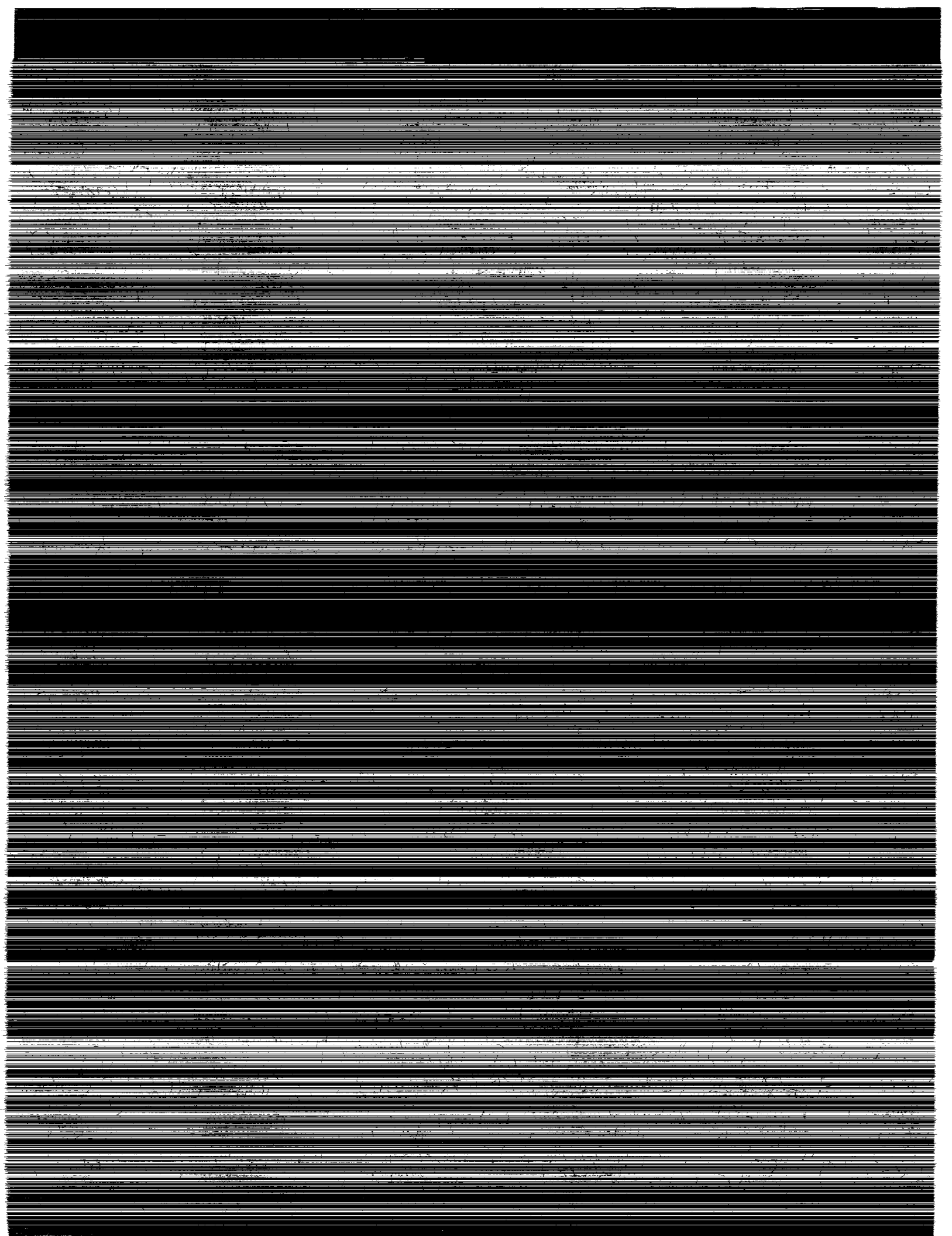
(NASA-TP-3385) INTERNAL
PERFORMANCE OF A NONAXISYMMETRIC
NOZZLE WITH A ROTATING UPPER FLAP
AND A CENTER-PIVOTED LOWER FLAP
(NASA) 59 p

N94-21569

Unclas

H1/02 0198097

NASA



**NASA
Technical
Paper
3385**

1993

**Internal Performance of a
Nonaxisymmetric Nozzle
With a Rotating Upper Flap
and a Center-Pivoted Lower Flap**

David J. Wing,
Laurence D. Leavitt,
and Richard J. Re
*Langley Research Center
Hampton, Virginia*



National Aeronautics and
Space Administration
Office of Management
Scientific and Technical
Information Program

Summary

An investigation was conducted at wind-off conditions in the static-test facility of the Langley 16-Foot Transonic Tunnel to determine the internal performance characteristics of a single expansion-ramp nozzle with thrust-vectoring capability to 105° . Thrust vectoring was accomplished by the downward rotation of an upper flap with adaptive capability for internal contouring and a corresponding rotation of a center-pivoted lower flap. The static internal performance of configurations with pitch thrust-vector angles of 0° , 60° , and 105° , each with two throat areas, was investigated. The nozzle pressure ratio was varied from 1.5 to approximately 8.0 (5.0 for the maximum throat area configurations). Results of this study indicated that the nozzle configuration of the present investigation, when vectored, provided excellent flow-turning capability with relatively high levels of internal performance. In all cases, the thrust-vector angle was a function of the nozzle pressure ratio. This result is expected because the flow is bounded by a single expansion surface on both vectored and unvectored nozzles.

Introduction

Recent efforts to expand the capabilities of fighter aircraft concentrate in part on vectored-thrust technology (ref. 1). High maneuverability and the capability of short takeoff and vertical landing (STOVL) are two benefits from these efforts that may be seen in near-future aircraft designs. Research into thrust-vectoring nozzles, that is, those that can deflect the thrust vector away from the engine centerline to produce controllable off-axis forces and moments, includes both axisymmetric (refs. 2 and 3) and nonaxisymmetric (refs. 4 to 21) designs. The nonaxisymmetric design is the configuration most suitable to the incorporation of thrust-vectoring schemes (ref. 22).

Two of the more extensively investigated non-axisymmetric nozzle designs are the two-dimensional convergent-divergent (2D-CD) nozzle and the single expansion-ramp nozzle (SERN). Of the two, the 2D-CD nozzle incorporates the more complete data base of the thrust-vectoring methods investigated (for example, refs. 4 to 12). The most efficient and promising means for deflecting the exhaust of a 2D-CD nozzle is probably the deflection of hinged, divergent flaps (ref. 23). Other methods that have also been attempted include upstream ports, post-exit vanes, and wedges. The data base on thrust-vectoring schemes for the SERN, however, is less extensive. Most efforts have concentrated on deflecting the divergent portions of the upper and lower ramps

in a manner similar to the 2D-CD nozzle (refs. 15 and 24). Limited thrust-vector angles, however, have been achieved by this method.

This report presents static internal performance data and pressure distribution data for a SERN capable of positive-pitch thrust vectoring to 105° (i.e., exhaust deflected down and forward). The thrust-vectoring concept was derived from an investigation of a nonaxisymmetric convergent nozzle reported in reference 25. Thrust vectoring is achieved by rotating the upper flap about a hinge point in the convergent section of the nozzle and pivoting the lower flap about a center point. The upper flap simulates a multibar linkage that can also adjust the internal contour. Design pitch-vector angles to 105° can be set, and the throat area can be varied for different power settings. Three design pitch-vector angles of 0° , 60° , and 105° were investigated, each at two throat areas. Nozzle pressure ratio was varied from 1.5 to approximately 8.0.

Symbols

All forces (except resultant gross thrust) and angles are referenced to the model centerline (body axis). A detailed discussion of data reduction procedures and equations is found in references 26 and 27.

A_t	total throat area of nozzle, in ²
F_a	measured thrust along body axis, lbf
F_i	ideal isentropic gross thrust, $w_p \left\{ \frac{R_j T_{t,j}}{g^2} \left(\frac{2\gamma}{\gamma-1} \right) \left[1 - \left(\frac{p_a}{p_{t,j}} \right)^{(\gamma-1)/\gamma} \right] \right\}^{1/2},$ lbf
F_n	measured normal force, lbf
F_r	resultant gross thrust, $\sqrt{F_a^2 + F_n^2}$, lbf
g	gravitational constant, 32.174 ft/sec ²
h_{ex}	for generic SERN, vertical distance from long ramp trailing edge to projection of short ramp trailing edge (see fig. 3(d)), in.
h_i	for generic SERN, vertical distance from short ramp trailing edge to long ramp (see fig. 3(d)), in.
h_t	for generic SERN, height of minimum flow passage (see fig. 3(d)), in.

$h_{t,a}$	nominal throat height on unvectored configurations and throat height of aft exhaust passage on vectored configurations (figs. 3(a) and 3(b)), in.
$h_{t,f}$	nominal throat height of forward exhaust passage on vectored configurations (fig. 3(b)), in.
i	sidewall orifice identification number
l_{ls}	total length along surface of lower fixed flap, 1.58 in.
l_{lrf}	total length along lower rotating flap axes (fig. 5(d)), 3.18 in.
l_{uf}	total length along surface of upper rotating flap (fig. 5), varies with flap configuration, in.
NPR	nozzle pressure ratio, $p_{t,j}/p_a$
p	local static pressure, psi
p_a	ambient pressure, psi
p_{swi}	local static pressure measured on right sidewall for each orifice number i , psi
p_{rswi}	local sidewall static-pressure ratio for each orifice number i , $p_{swi}/p_{t,j}$, psi
$p_{t,j}$	jet total pressure, psi
R_j	gas constant for air ($\gamma = 1.3997$), $1716 \text{ ft}^2/\text{sec}^2\text{-}^\circ\text{R}$
$T_{t,j}$	jet total temperature, $^\circ\text{R}$
x	dimension along surface of upper rotating flap (fig. 3(a)), in.
x'	dimension along surface of lower fixed flap (fig. 3(a)), in.
x''	dimension along longitudinal axis of the lower rotating flap (fig. 3(a)), in.
w_i	ideal weight-flow rate, $p_{t,j} A_t \left(\frac{\gamma g}{T_{t,j} R_j} \right)^{1/2} \left(\frac{2}{\gamma + 1} \right)^{(\gamma + 1)/2(\gamma - 1)},$ lb/ft ² /sec
w_p	measured weight-flow rate, lb/ft ² /sec
δ_p	resultant thrust-vector angle, $\tan^{-1}(F_n/F_a)$, deg

δ_v	design thrust-vector angle, deg
ε_{ex}	estimated external-expansion ratio h_{ex}/h_t for constant width nozzle
ε_i	estimated internal-expansion ratio h_i/h_t for constant width nozzle
γ	ratio of specific heats, 1.3997 for air
θ_l	lower flap angle of rotation (fig. 3), deg
θ_u	upper flap angle of rotation (fig. 3), deg

Abbreviations:

A/B	afterburning
Config	configuration
max	maximum
min	minimum
SERN	single expansion-ramp nozzle
Sta.	station
STOVL	short takeoff and vertical landing
typ	typical
WL	waterline
2D-CD	two-dimensional convergent-divergent

Apparatus and Methods

Static-Test Facility

This investigation was conducted in the static-test facility of the Langley 16-Foot Transonic Tunnel. The jet exhaust was released to the atmosphere. This facility utilizes the same clean dry-air supply as that used for jet simulation in the Langley 16-Foot Transonic Tunnel and a similar air control system, including valves, filters, and a heat exchanger to operate the jet flow at a constant stagnation temperature (ref. 26).

Single-Engine Propulsion Simulation System

A sketch of the single-engine air-powered nacelle model on which various nozzles were mounted is presented in figure 1 with a typical nozzle configuration attached. An external high-pressure air system provided a continuous flow of clean dry air at a controlled temperature of about 530°R . This high-pressure air was brought through a dolly-mounted support strut by six tubes that connect to a high-pressure plenum chamber. As shown in figure 1, the air was then discharged perpendicularly into the

low-pressure plenum. This method was designed to minimize forces imposed by the transfer of axial momentum as the air is passed from the nonmetric high-pressure plenum to the metric (mounted to the force balance) low-pressure plenum. Two flexible metal bellows are used as seals and serve to compensate for axial forces caused by pressurization. The air was then passed from the low-pressure plenum (circular in cross section) through a transition section, a choke plate, and an instrumentation section. The transition section provided a smooth flow path for the airflow from the round low-pressure plenum to the rectangular choke plate and instrumentation section. The instrumentation section had a flow-path width-to-height ratio of 1.437 and was identical in geometry to the nozzle airflow entrance. The nozzles were attached to the instrumentation section at model station (Sta.) 41.13.

Nozzle Design

A photograph of a typical nonaxisymmetric nozzle installed on the single-engine propulsion system is shown in figure 2. Photographs and sketches of the six test nozzle configurations and their components are shown in figures 3 through 6. The unvectored (cruise) nozzle (fig. 3(a)) is a single expansion-ramp nozzle (SERN) because the divergent flaps are of unequal length. As the name implies, only one external surface provides a solid boundary for a portion of the external flow expansion. Sidewall containment on this nozzle was approximately 50 percent of the divergent passage length, where length is based on the upper flap length. Each of the three vector-angle configurations was tested with two throat areas that simulated two power settings, for a total of six configurations. These configurations are illustrated in figure 3. The minimum and maximum throat area configurations, as they will be called in this report, correspond, respectively, to a dry (military) power setting and a maximum afterburning (A/B) power setting. Furthermore, in each vector-angle configuration, only the upper pitch flap is modified in shape to provide the change in power setting. Definitions of internal- and external-expansion ratios for a generic single expansion-ramp nozzle are given in figure 3(d). These definitions were used to estimate the expansion ratios tabulated in figure 3(c) for each flow passage of the current nozzle.

Thrust vectoring is accomplished by the simultaneous rotation of the upper flap about a hinge point (Sta. 45.48) in the convergent section of the nozzle and the lower flap about a center pivot point. The upper flap represents a multibar linkage that can adjust the internal contour. For purposes of model sim-

plicity, separate solid upper flaps were constructed instead of moving parts. Design thrust-vector angles of 60° and 105° were tested in addition to the unvectored nozzle. With the exception of the unvectored nozzle, the lower rotating flap angle was equal to the design thrust-vector angle.

Two flow passages are formed by the rotation of the lower flap. They are labeled in this report as the aft and forward passages. The aft passage is bounded by the upper flap and the lower rotating flap, and the forward passage is bounded by the lower (or upstream) surface of the lower rotating flap and the fixed lower flap. One exception is the minimum throat area, thrust-vectoring configuration of 105° , where the aft passage was completely closed. Estimated internal- and external-expansion ratios for each passage are tabulated in figure 3(c).

Instrumentation

A three-component strain-gauge balance was used to measure the forces and moments on the model. (See fig. 1.) Jet total pressure was measured at a fixed station in the instrumentation section by a four-probe rake through the upper surface, a three-probe rake through the side, and a three-probe rake through the corner. A thermocouple, also located in the instrumentation section, was used to measure jet total temperature. A weight-flow rate of the high-pressure air supplied to the nozzle was determined by calibrating weight flow as a function of pressure and temperature measurements in the high-pressure plenum (located on top of the support strut) with standard axisymmetric nozzles of known discharge coefficient in place of the test nozzle. Internal static-pressure orifices were located on all fixed- and rotating-flap hardware and on the right sidewall. (See fig. 6.) The static-pressure orifices on the nozzle flaps (both fixed and rotating) were located in a single row along the centerline. Actual locations of these orifices are given in tables 1 to 6.

Three coordinate systems were used in this report to define pressure tap locations. The x -coordinate system is used to define pressure tap locations for the upper rotating flap. This coordinate system follows the surface of the upper rotating flap as shown in figures 3 and 5. Positive x is defined as downstream. The x' -coordinate system is used to define pressure orifice locations on the fixed lower flap. This system also follows the surface of the flap and is shown in figure 3(a). The origin of this system begins at Sta. 43.03, and x' is positive downstream. The x'' -coordinate system is used to define pressure orifice locations on the lower rotating flap. Unlike the other two systems, the x'' system lies along the

axes defining the lower rotating flap, as shown in figure 5(d), rather than along the surface contour. Positive x'' is defined as downstream.

Data Reduction

All data were recorded simultaneously on magnetic tape. Approximately 50 frames of data, taken at a rate of 10 frames per second, were used for each data point; average values were used in computations. Data were recorded in ascending order of $p_{t,j}$. Except for resultant thrust F_r , all force data in this report are referenced to the model centerline.

The basic internal performance parameters used for the presentation of results are F_a/F_i , F_r/F_i , δ_p , and w_p/w_i . The axial thrust ratio F_a/F_i is the ratio of measured nozzle thrust (along the body axis) to ideal nozzle thrust, where ideal nozzle thrust is based on measured weight-flow rate, total temperature, and total pressure in the instrumentation section. The balance axial-force measurement, from which nozzle thrust was obtained, was initially corrected for model weight tares and balance interactions. Although the bellows arrangement was designed to eliminate pressure and momentum interactions with the balance, small bellows tares on axial, normal, and pitch balance components still existed. These residual tares resulted from a small pressure difference between the ends of the bellows when internal velocities were high and from small differences in the forward and aft bellows spring constants when the bellows were pressurized. As described in reference 26, the bellows tares were determined by testing calibration nozzles with known performance over a range of expected normal forces and pitching moments. The balance data were then corrected in a manner discussed in reference 27 to obtain actual nozzle thrust, normal force, and pitching moment. The resultant thrust F_r and the resultant thrust-vector angle δ_p were then determined from the corrected balance data.

The resultant thrust ratio F_r/F_i is equal to the axial thrust ratio F_a/F_i as long as the jet-exhaust flow remains unvectoring ($\delta_p = 0^\circ$). Significant differences between F_r/F_i and F_a/F_i occur when jet-exhaust flow is turned from the axial direction; the magnitude of these differences is a function of δ_v and NPR. The nozzle discharge coefficient w_p/w_i is the ratio of measured weight-flow rate to ideal weight-flow rate, where ideal weight-flow rate is based on jet total pressure $p_{t,j}$, jet total temperature $T_{t,j}$, and measured nozzle throat area.

Discussion of Results

Data are presented in both tabular and graphical formats. The data for nozzle internal static-pressure

ratios are presented in tabular form in tables 1 to 6. Data on nozzle performance characteristics are presented in table 7 for all configurations tested. The data analysis figures and the ensuing discussion of experimental results are divided into discussions of the unvectoring-nozzle performance (figs. 7 to 10), the $\delta_v = 60^\circ$ nozzle performance (figs. 11 to 14), and the $\delta_v = 105^\circ$ nozzle performance (figs. 15 to 18). A summary of nozzle performance characteristics as a function of thrust-vector angle is presented in figure 19.

Unvectoring Nozzle, $\delta_v = 0^\circ$

In the cruise (unvectoring) configuration, the nozzle has the geometry of a single expansion-ramp nozzle (SERN), which is a 2D-CD nozzle with divergent ramps of unequal length. The internal performance of nozzles with SERN geometry has been established in previous research and can be found in references 13 to 17, which include detailed discussions on the behavior of single expansion-ramp nozzles. Nozzle internal performance characteristics for the unvectoring-nozzle configurations are presented in figure 7. Data on upper and lower flap surface pressure ratios are provided in figures 8 and 9, and typical nozzle sidewall pressure ratio contours are presented in figure 10.

Nozzle performance characteristics for the unvectoring-nozzle configurations are presented in figure 7 as a function of NPR. The resultant thrust ratio variation is typical of SERN nozzles because the peak performance is spread out over a wide range of NPR and is a function of both the internal- and external-expansion ratios. The peak thrust ratio of about 0.975 generated by the unvectoring configurations is considered typical for this exhaust nozzle class. The effect of differences in external-expansion ratio is illustrated by the fact that the maximum area nozzle reached peak performance at a value of NPR well below that of the minimum area configuration.

The thrust-vector angle in the pitch plane δ_p is calculated from the individually measured components of thrust. Relatively large negative resultant thrust-vector angles were measured, particularly at the overexpanded flow condition (values of NPR below the NPR for fully expanded flow, which is the design NPR). This behavior is a typical SERN nozzle characteristic. As NPR approaches the design level, resultant thrust-vector angles typically decrease to near 0° . Positive values of thrust-vector angle generally occur for nozzle pressure ratios above the NPR for fully expanded flow on the nozzle external surface. As seen in figure 7, smaller values of thrust-vector angle were generated by the maximum area

configuration than by the minimum area configuration. For a given nozzle pressure ratio, the maximum area configuration is operating nearer the design condition than the minimum area configuration. A comparison of the axial thrust ratio F_a/F_i with the resultant thrust ratio shows that axial thrust is generally sacrificed at lower NPR because of the large vectored-thrust angles generated.

Nozzle discharge coefficient is a measure of the actual weight flow compared with an ideal weight flow, where the ideal weight flow is based on the geometric throat area. The low values of discharge coefficient measured on the minimum area nozzle configuration (relative to those measured for the maximum area configuration) indicate substantial losses in effective throat area. These losses are believed to be a result of the momentum and vena contracta losses associated with the extreme convergence angle on the upper flap.

Evidence of such flow can be inferred from the data for centerline pressure ratios that are presented in figure 8. The centerline static-pressure ratio distributions along the upper (longer) ramp are plotted for both the minimum and maximum throat area configurations (dry and A/B power, respectively). Considering the minimum area configuration first, an abrupt expansion of the flow occurred in the region around $x/l_{uf} = 0.3$ (between the sixth and seventh pressure taps). The seventh tap, counted in the downstream direction, was located at the station of minimum flow area in the nozzle (the geometric throat). In theory, a static-pressure ratio of $p/p_{t,j} = 0.528$ corresponds to sonic flow. Therefore, the effective throat location is slightly upstream of the geometric throat location on the upper surface of the nozzle. The abrupt expansion at the throat corner was followed by an overexpansion to a lower static-pressure ratio. This characteristic is typical for nozzles that require the flow to turn through large angles at the throat. Generally, a small separated region, characterized by low static pressure, forms immediately downstream of the throat because the flow fails to remain attached to the surface. This overexpansion is typically followed by pressure recovery to ambient pressure values ($p_a/p_{t,j}$). By comparison, the maximum area configuration experiences a more benign expansion (higher initial velocities, less severe surface angles, therefore, less overexpansion downstream of the throat) on the upper surface, which is consistent with the smaller flow contraction ahead of the geometric throat. The stations of minimum flow area for the minimum and maximum area configurations correspond to the seventh and sixth pressure taps, respectively, as counted in the downstream direction.

The sonic line ($p/p_{t,j} = 0.528$) was located slightly upstream of the geometric throat on the upper flap, as was the case for the minimum area configuration.

When interpreting the pressure distributions in this report, one should consider that the data are plotted and faired by computer, and fairings in regions of large gradients may not accurately represent the true behavior in the nozzle between pressure taps. As an example, in figure 8 for the minimum area configuration at NPR = 1.5, the flow probably expands to a static-pressure ratio below 0.528 between the sixth and seventh pressure taps, although this behavior is not shown in the fairing.

Lower rotating flap pressure distributions are presented in figure 9. Both throat area configurations exhibited a relatively smooth acceleration over the entire lower flap. For NPR's above 1.5, sonic flow was reached at a location of approximately 85 percent of the lower flap length, hence, was near the trailing edge. Note that the static-pressure ratio values on the maximum area configuration were generally lower than on the minimum area configuration, indicating higher flow velocities.

Contour plots of sidewall static-pressure ratios are presented for both throat area configurations in figure 10. An important consideration in viewing the contour plots in this report is the limited number of pressure measurements available for calculating the contours. The contours presented were formed using a combination of sidewall static-pressure measurements coupled with centerline static pressures on both the upper and lower flaps. This method, which is identical to that presented in reference 25, assumes that the flow is generally 2D. The contour plot results should be used in a qualitative rather than a quantitative manner because actual pressure contours in a given vertical plane differ in detail from the contours presented.

In figure 10, data are presented at two values of NPR, one at NPR = 3.0 and one at a value of NPR near the design point that is based on the external-expansion ratio. For the minimum area configuration (figs. 10(a) and (b)), the abrupt expansion (i.e., flow acceleration) near the throat radius on the upper surface can be seen relative to the smooth acceleration on the lower surface. From the discussion of centerline pressure distributions (fig. 8), a local region of acceleration was noted on the upper flap just downstream of the minimum flow area station and was followed by a small recovery. The sonic plane ($p/p_{t,j} = 0.528$) was clearly inclined relative to the nozzle centerline, and the lower surface intersection

occurred downstream, resulting in the negative values of thrust-vector angle discussed earlier. As illustrated in references 13 and 15, this result is common in SERN nozzle designs. When the NPR is increased to values greater than those tested, a reversal in the sign of the resultant thrust-vector angle occurs as flow becomes underexpanded (and pressures become greater than ambient pressure) on the upper flap.

The pressure contour plots for the maximum area configuration in figures 10(c) and (d) pictorially show the more gradual expansion on the upper surface near the throat. Again, the sonic plane is inclined with the lower edge farther downstream.

Thrust-Vectored Nozzle, $\delta_v = 60^\circ$

The nozzle in a $\delta_v = 60^\circ$ thrust-vectoring configuration has two separate flow passages (fig. 3(c)). For the discussion presented herein, these flow passages are referred to as the forward and aft passages. The forward passage has the geometry of a SERN, where the lower surface of the lower rotating flap serves as an external-expansion surface. The aft passage is typical of a high-aspect ratio, 2D-CD nozzle with divergent surfaces of nearly equal length. The minimum and maximum area nozzles differ geometrically only in the aft passage.

Nozzle performance characteristics for the $\delta_v = 60^\circ$ thrust-vectored nozzles are presented in figure 11. Values of resultant thrust ratio were generally between 0.97 and 0.99. Two important characteristics are noted: (1) the resultant thrust ratio remained relatively high for both configurations over the entire range of NPR and (2) evidence exists that overall nozzle performance characteristics are a composite of both forward and aft passage performance characteristics. As noted in the previous paragraph, the forward passage, which is identical for both area variations, has an internal-expansion ratio of 1.0 and an external-expansion ratio of approximately 1.1. Peak performance in this passage is expected at NPR values between 2.0 and 3.0. The aft passage geometry is a function of configuration. The minimum area configuration creates an aft passage with a high internal expansion ratio (approximately 2.0, design NPR ≈ 11.0). The maximum area configuration results in an aft passage with a considerably smaller internal expansion ratio of approximately 1.3 (design NPR ≈ 5.0). As seen in figure 11, evidence indicates that multiple performance peaks exist. The early peak occurs at an NPR of approximately 2.0 for both area configurations. The second peak would occur at a lower NPR for the maximum area configuration than for the minimum area configuration.

These observations appear to be consistent with the configuration differences discussed.

Flow expansion in the aft passage can be further illustrated by examination of the centerline pressure distributions on the upper flap (fig. 12) and on the aft surface of the lower rotating flap (fig. 13). The expansion process of the minimum area configuration is considerably more rapid, as indicated by the steep fairing downstream of x/l_{uf} and $x''/l_{rf} = 0.4$. For complete expansion in the nozzle (NPR > 5.0 for the minimum area configuration, and NPR > 2.0 for the maximum area configuration), pressure expands to a lower minimum value than that value measured for the maximum area configuration. Rapid recovery from these low pressures often results in flow separation on the divergent sections of the flaps, causing performance losses.

Both nozzle configurations provided excellent resultant thrust-vector angles relative to the geometric vector angle of 60° . As seen in figure 11, the resultant thrust-vector angle was a strong function of NPR. This result is typical of SERN nozzle operation (ref. 13). After the NPR for fully expanded external flow in the forward passage is reached, further increases in NPR result in increased flow turning on the unbounded expansion surface (forward surface of the lower rotating flap). In all cases, the resultant thrust-vector angle was greater than 57° . As expected, the axial thrust ratio values mirror the turning angle results. The axial thrust ratio F_a/F_i decreases as the resultant thrust-vector angle increases and as flow is turned from the axial direction.

The discharge coefficients of both nozzle area configurations were high and generally constant with NPR, indicating a stable throat location with little reduction in effective throat area.

The pressure contour data presented in figure 14 are consistent with the above discussions. Except for local areas of accelerated flow, apparently nozzle flow is turned at subsonic speeds when static-pressure ratio values are relatively high (i.e., Mach number is low). When the predominant flow-turning mechanism does occur at subsonic speeds, resultant thrust ratio values are generally high, which is the case for both configurations at $\delta_v = 60^\circ$. One additional point to make from these pressure contour plots is the inclination of the sonic line (throat) in the forward passage. That is, the sonic line attaches considerably farther upstream on the fixed lower flap than on the upstream surface of the lower rotating flap. This additional rotation (more than 60°) of the throat efflux, coupled with the pressures on the

external-expansion surface, helps explain the large resultant thrust-vector angles presented in figure 11.

Thrust-Vectored Nozzle, $\delta_v = 105^\circ$

The minimum area $\delta_v = 105^\circ$ configuration is unique because the upper rotating flap completely closes the aft exhaust passage. All exhaust flow, therefore, is directed through the forward exhaust passage formed between the fixed lower flap and the forward surface of the lower rotating flap. As discussed previously, the lower rotating flap provides an unbounded external-expansion surface for the exhaust flow. The maximum area configuration, conversely, has both forward and aft exhaust passages. The lower rotating flap forms an external-expansion surface for both passages. Nozzle performance characteristics are presented in figure 15. Various data on static-pressure ratios (centerline distributions and sidewall contours) are presented in figures 16 to 18.

Resultant thrust ratio values for the $\delta_v = 105^\circ$ vectoring configurations (fig. 15) generally indicate lower performance than the performance measured for the unvectored or $\delta_v = 60^\circ$ vectoring configurations. The results, however, are consistent with those measured on similar vertical thrust nozzles and thrust reversers (refs. 8 and 28). Peak performance for the minimum area configuration occurs at an NPR of approximately 2.0. The occurrence of peak performance at this low NPR is typical of a convergent exhaust nozzle. For the upstream flow passage of both the minimum and maximum area configurations, the upstream end of the sonic line is probably located at the exit corner of the fixed lower flap, and the downstream end is located within the last 25 percent of the lower rotating flap. (See fig. 17.) Therefore, for both configurations, the sonic line for the upstream flow passage is most likely skewed relative to the flow passage centerline. When such a small portion of external-expansion surface remains, the flow passage is essentially a convergent nozzle, which is consistent with the performance behavior of the minimum area nozzle (fig. 15).

The maximum area nozzle, however, has an additional flow path that has the geometry of a SERN. The pressure distributions in figures 16 and 17 show that the sonic line is located well inside the flow passage. The resultant thrust ratio curve in figure 15 shows behavior more typical of a SERN than of a convergent nozzle, which suggests that the aft passage significantly affects the performance of the entire nozzle.

Resultant thrust ratio values (fig. 15) measured for the maximum area configuration at low NPR values are considerably lower than those measured for

the minimum area configuration and are indicative of overexpanded flow conditions. Both internal- and external-expansion ratios are large for the aft passage of the maximum area configuration at $\delta_v = 105^\circ$, so large that the NPR for fully expanded flow in the aft passage could not be attained. In fact, the flow appears to be fully separated from the aft surface of the lower rotating flap at values of NPR above 2.0, as shown in figure 17, where static-pressure ratio values downstream of $x''/l_{\text{trf}} = 0.4$ are relatively constant and approximately equal to ambient.

The resultant thrust-vector angle was, in general, lower than the design value of 105° for an NPR less than about 4.0. As noted previously, a strong dependence on NPR was measured, a characteristic typical of nozzles that employ external expansion. Resultant thrust-vector angles ranged from 97° to approximately 110° for the NPR range tested.

The axial thrust ratio shown in figure 15 is significant in that negative values of F_a/F_i indicate that thrust is directed forward of vertical (reverse thrust). As seen, reverse thrust levels generally increased as the NPR increased.

Nozzle discharge coefficient (fig. 15) levels are lower for configurations in which $\delta_v = 105^\circ$ than for either the unvectored or vectoring configurations in which $\delta_v = 60^\circ$. Variation with the NPR suggests that the throat location and/or shape varies because of viscous-separation phenomena. Evidence of this movement can be inferred from static-pressure ratio data provided in tables 5 and 6 for the forward surface of the lower rotating flap.

Effects of Design Thrust-Vector Angle

A summary of the effects of design thrust-vector angle on resultant thrust ratio and thrust-vector angle is shown in figure 19. Data are presented for NPR = 3.0, a typical value for takeoff and landing conditions. As seen, nozzle resultant thrust performance is a function of thrust-vector angle and is highest for the $\delta_v = 60^\circ$ vectoring case. For the typical thrust-vectoring nozzle concept, nozzle performance usually decreases with increases in nozzle thrust-vector angle. For this investigation, although the thrust-vectoring configurations are all geometric variations from a single nozzle concept, each configuration results in unique internal geometry. These unique geometries, therefore, may or may not have related performance levels. As a result, interpolation of performance as a function of thrust-vector angle may not be appropriate.

Relatively high performance levels for all vectoring configurations are, at least in part, a result of

flow turning at subsonic speeds. Subsonic flow turning has long been linked with high thrust-vector nozzle performance.

At the NPR presented, the measured thrust-vector angles were, in general, less than or equal to the design thrust-vector angles. The largest deviation occurred at $\delta_v = 0^\circ$. The large negative thrust-vector angle for the unvectorized configurations was attributed to throat inclination and the external-expansion surface pressure distribution. The maximum area configurations at NPR = 3.0 generally provided slightly higher thrust-vector angles than the minimum area configurations provided.

Conclusions

An investigation was conducted at wind-off conditions in the static-test facility of the Langley 16-Foot Transonic Tunnel to determine the internal performance characteristics of a single expansion-ramp nozzle with thrust-vectoring capability to 105° . Thrust vectoring was accomplished by the downward rotation of an upper flap with adaptive capability for internal contouring and a corresponding rotation of a center-pivoted lower flap. The static internal performance of configurations with pitch thrust-vector angles of 0° , 60° , and 105° , each with two throat areas, was investigated. Nozzle pressure ratio was varied from 1.5 to approximately 8.0 (5.0 for the maximum throat area configurations). The results of this study indicate the following conclusions:

1. The cruise configuration provided relatively constant internal static thrust performance for nozzle pressure ratio values above 3.0. Peak resultant thrust ratio levels of 0.975, which are considered typical for this class of exhaust nozzle, were measured. The unvectorized nozzle produced negative thrust-vector angles at all values of nozzle pressure ratio tested.
2. The nozzle provided excellent resultant thrust performance levels when vectorized. The $\delta_v = 60^\circ$ configuration, in fact, performed more efficiently than either the unvectorized- (cruise) or the $\delta_v = 105^\circ$ vectorized-thrust configurations. Resultant thrust ratio performance levels for the $\delta_v = 60^\circ$ configurations were relatively constant throughout the nozzle pressure ratio range tested.
3. The thrust-vectoring scheme utilized in this investigation created dual exhaust flow passages except for the minimum area at the $\delta_v = 105^\circ$ configuration. As a result, performance characteristics of the vectorized configurations were generally a composite of the individual exhaust passage characteristics.

4. The vectorized configurations provided excellent flow-turning capability. Measured resultant thrust-vector angles were generally close to the design thrust-vector angles for the vectorized configurations. However, the unvectorized configurations produced negative thrust-vector angles, which are typical for a single expansion-ramp nozzle operating below the design condition. In all cases, the thrust-vector angle was a function of the nozzle pressure ratio. This result is expected because the flow is bounded by a single expansion surface on both vectorized- and unvectorized-nozzle geometries.

NASA Langley Research Center
Hampton, VA 23681-0001
July 2, 1993

References

1. Bitten, R.; and Selmon, J.: Operational Benefits of Thrust Vector Control (TVC). *High-Angle-of-Attack Technology, Volume 1*, Joseph R. Chambers, William P. Gilbert, and Luat T. Nguyen, eds., NASA CP-3149, Part 2, 1992, pp. 587-601.
2. Berrier, Bobby L.; and Mason, Mary L.: *Static Performance of an Axisymmetric Nozzle With Post-Exit Vanes for Multiaxis Thrust Vectoring*. NASA TP-2800, 1988.
3. Carson, George T., Jr.; and Capone, Francis J.: *Static Internal Performance of an Axisymmetric Nozzle With Multiaxis Thrust-Vectoring Capability*. NASA TM-4237, 1991.
4. Taylor, John G.: *Static Investigation of a Two-Dimensional Convergent-Divergent Exhaust Nozzle With Multiaxis Thrust-Vectoring Capability*. NASA TP-2973, 1990.
5. Capone, Francis J.; Mason, Mary L.; and Leavitt, Laurence D.: *An Experimental Investigation of Thrust Vectoring Two-Dimensional Convergent-Divergent Nozzles Installed in a Twin-Engine Fighter Model at High Angles of Attack*. NASA TM-4155, 1990.
6. Mason, Mary L.; and Berrier, Bobby L.: *Static Performance of Nonaxisymmetric Nozzles With Yaw Thrust-Vectoring Vanes*. NASA TP-2813, 1988.
7. Capone, Francis J.; and Bare, E. Ann: *Multiaxis Control Power From Thrust Vectoring for a Supersonic Fighter Aircraft Model at Mach 0.20 to 2.47*. NASA TP-2712, 1987.
8. Mason, Mary L.; and Burley, James R., II: *Static Investigation of Two STOL Nozzle Concepts With Pitch Thrust-Vectoring Capability*. NASA TP-2559, 1986.
9. Re, Richard J.; and Leavitt, Laurence D.: *Static Internal Performance of a Thrust Vectoring and Reversing Two-Dimensional Convergent-Divergent Nozzle With an Aft Flap*. NASA TP-2549, 1986.

10. Capone, Francis J.; and Carson, George T., Jr.: *Effects of Empennage Surface Location on Aerodynamic Characteristics of a Twin-Engine Afterbody Model With Non-axisymmetric Nozzles*. NASA TP-2392, 1985.
11. Re, Richard J.; and Leavitt, Laurence D.: *Static Internal Performance Including Thrust Vectoring and Reversing of Two-Dimensional Convergent-Divergent Nozzles*. NASA TP-2253, 1984.
12. Bare, E. Ann; and Berrier, Bobby L.: *Investigation of Installation Effects on Twin-Engine Convergent-Divergent Nozzles*. NASA TP-2205, 1983.
13. Re, Richard J.; and Leavitt, Laurence D.: *Static Internal Performance of Single-Expansion-Ramp Nozzles With Various Combinations of Internal Geometric Parameters*. NASA TM-86270, 1984.
14. Mason, Mary L.; and Capone, Francis J.: *Aeropropulsive Characteristics of Twin Single-Expansion-Ramp Vectoring Nozzles Installed With Forward-Swept Wings and Canards*. NASA TP-2133, 1983.
15. Re, Richard J.; and Berrier, Bobby L.: *Static Internal Performance of Single Expansion-Ramp Nozzles With Thrust Vectoring and Reversing*. NASA TP-1962, 1982.
16. Berrier, Bobby L.; and Re, Richard J.: *Effect of Several Geometric Parameters on the Static Internal Performance of Three Nonaxisymmetric Nozzle Concepts*. NASA TP-1468, 1979.
17. Berrier, Bobby L.; and Leavitt, Laurence D.: *Static Internal Performance of Single-Expansion-Ramp Nozzles With Thrust Vectoring Capability up to 60°*. NASA TP-2364, 1984.
18. Taylor, John G.: *Internal Performance of a Hybrid Axisymmetric/Nonaxisymmetric Convergent-Divergent Nozzle*. NASA TM-4230, 1991.
19. Berrier, Bobby L.; and Taylor, John G.: *Internal Performance of Two Nozzles Utilizing Gimbal Concepts for Thrust Vectoring*. NASA TP-2991, 1990.
20. Carson, George T., Jr.; and Lamb, Milton: *Aeropropulsive Characteristics of Isolated Combined Turbojet/Ramjet Nozzles at Mach Numbers From 0 to 1.20*. NASA TP-2814, 1988.
21. Capone, Francis J.; and Reubush, David E.: *Effects of Varying Podded Nacelle-Nozzle Installations on Transonic Aeropropulsive Characteristics of a Supersonic Fighter Aircraft*. NASA TP-2120, 1983.
22. Berrier, B. L.; and Re, R. J.: *A Review of Thrust-Vectoring Schemes for Fighter Aircraft*. AIAA Paper No. 78-1023, July 1978.
23. Berrier, Bobby L.: *Results from NASA Langley Experimental Studies of Multiaxis Thrust Vectoring Nozzles*. SAE Tech. Paper Ser. 881481, Oct. 1988.
24. Capone, Francis J.; and Schirmer, Alberto W.: *Static Internal Performance of a Single Expansion Ramp Nozzle With Multiaxis Thrust Vectoring Capability*. NASA TM-4450, 1993.
25. Leavitt, Laurence D.: *Static Internal Performance of a Two-Dimensional Convergent Nozzle With Thrust-Vectoring Capability up to 60°*. NASA TP-2391, 1985.
26. *A User's Guide to the Langley 16-Foot Transonic Tunnel Complex, Revision 1*. NASA TM-102750, 1990. (Supersedes NASA TM-83186, compiled by Kathryn H. Peddrew, 1981.)
27. Mercer, Charles E.; Berrier, Bobby L.; Capone, Francis J.; Grayston, Alan M.; and Sherman, C. D.: *Computations for the 16-Foot Transonic Tunnel—NASA, Langley Research Center, Revision 1*. NASA TM-86319, 1987. (Supersedes NASA TM-86319, 1984.)
28. Berrier, Bobby L.; and Capone, Francis J.: *Effect of Port Corner Geometry on the Internal Performance of a Rotating-Vane-Type Thrust Reverser*. NASA TP-2624, 1986.

Table 1. Nozzle Internal Static-Pressure Ratios

$[\delta_v = 0^\circ, \text{ minimum area configuration}]$

(a) Upper flap centerline

x/l_{uf}													
NPR	-0.26	-0.17	-0.07	0.10	0.19	0.28	0.37	0.47	0.56	0.65	0.74	0.84	0.93
1.50	0.983	0.984	0.986	0.993	0.978	0.939	0.562	0.578	0.576	0.591	0.611	0.632	0.649
1.76	.981	.982	.983	.992	.975	.931	.438	.453	.460	.487	.513	.535	.553
2.00	.980	.981	.982	.991	.973	.928	.299	.349	.361	.398	.437	.469	.491
2.27	.980	.981	.981	.991	.973	.926	.213	.246	.284	.345	.394	.429	.449
2.51	.980	.981	.981	.991	.972	.926	.204	.139	.241	.304	.455	.499	.443
3.00	.980	.980	.981	.991	.972	.926	.203	.139	.240	.260	.246	.406	.453
4.02	.978	.980	.981	.989	.970	.924	.202	.141	.237	.258	.234	.198	.160
5.01	.978	.980	.981	.988	.970	.923	.200	.141	.234	.256	.232	.198	.159
6.00	.977	.980	.981	.987	.969	.922	.199	.139	.232	.254	.231	.197	.160
7.00	.977	.980	.981	.986	.968	.922	.198	.136	.229	.252	.230	.197	.160
8.00	.977	.980	.981	.985	.968	.921	.196	.134	.226	.249	.229	.196	.160

(b) Lower fixed flap centerline

x'/l_{lf}			
NPR	0.32	0.56	0.78
1.50	0.978	0.980	0.983
1.76	.975	.977	.981
2.00	.974	.976	.979
2.27	.973	.975	.979
2.51	.973	.975	.979
3.00	.972	.975	.979
4.02	.972	.974	.978
5.01	.972	.973	.978
6.00	.971	.973	.977
7.00	.971	.971	.976
8.00	.970	.970	.975

Table 1. Concluded

(c) Top surface centerline of lower rotating flap

$$x''/l_{\text{rf}}$$

NPR	0.05	0.18	0.30	0.42	0.54	0.67	0.79	0.92
1.50	0.988	0.974	0.958	0.909	0.875	0.818	0.715	0.637
1.76	.985	.971	.953	.898	.858	.787	.652	.526
2.00	.984	.969	.951	.894	.850	.771	.618	.466
2.27	.984	.969	.950	.892	.845	.763	.598	.434
2.51	.984	.969	.950	.892	.845	.762	.594	.413
3.00	.983	.969	.949	.892	.844	.761	.593	.413
4.02	.980	.968	.948	.890	.841	.760	.591	.413
5.01	.978	.967	.947	.888	.839	.759	.590	.412
6.00	.977	.966	.946	.885	.837	.756	.588	.412
7.00	.976	.965	.945	.881	.835	.753	.587	.412
8.00	.976	.964	.944	.878	.832	.751	.585	.411

(d) Right sidewall

NPR	$pr_{\text{sw}2}$	$pr_{\text{sw}4}$	$pr_{\text{sw}5}$	$pr_{\text{sw}6}$	$pr_{\text{sw}7}$	$pr_{\text{sw}8}$	$pr_{\text{sw}9}$	$pr_{\text{sw}10}$	$pr_{\text{sw}11}$	$pr_{\text{sw}12}$	$pr_{\text{sw}17}$	$pr_{\text{sw}18}$	$pr_{\text{sw}19}$
1.50	0.974	0.974	0.971	0.978	0.975	0.963	0.978	0.974	0.968	0.960	0.981	0.973	0.962
1.76	.972	.972	.969	.976	.973	.960	.976	.971	.966	.957	.980	.971	.958
2.00	.971	.971	.967	.975	.972	.958	.975	.970	.964	.956	.979	.970	.964
2.27	.971	.971	.967	.975	.971	.957	.975	.970	.963	.955	.979	.970	.966
2.51	.971	.971	.967	.975	.971	.957	.975	.970	.964	.955	.979	.970	.968
3.00	.970	.971	.967	.975	.971	.957	.974	.969	.963	.955	.978	.970	.968
4.02	.969	.970	.966	.973	.969	.956	.973	.968	.962	.954	.977	.969	.969
5.01	.968	.969	.965	.972	.969	.955	.972	.967	.961	.953	.977	.968	.970
6.00	.967	.968	.964	.971	.968	.954	.971	.966	.960	.952	.976	.967	.969
7.00	.965	.967	.963	.969	.966	.952	.970	.964	.958	.950	.975	.966	.969
8.00	.964	.965	.961	.967	.964	.951	.969	.963	.957	.949	.973	.964	.968

NPR	$pr_{\text{sw}20}$	$pr_{\text{sw}21}$	$pr_{\text{sw}22}$	$pr_{\text{sw}23}$	$pr_{\text{sw}25}$	$pr_{\text{sw}26}$	$pr_{\text{sw}27}$	$pr_{\text{sw}28}$	$pr_{\text{sw}29}$	$pr_{\text{sw}35}$	$pr_{\text{sw}36}$	$pr_{\text{sw}37}$
1.50	0.965	0.958	0.949	0.940	0.905	0.888	0.922	0.932	0.722	0.588	0.651	0.617
1.76	.962	.954	.945	.934	.896	.879	.913	.912	.669	.474	.571	.494
2.00	.961	.953	.942	.931	.892	.875	.909	.901	.635	.380	.517	.420
2.27	.960	.952	.941	.929	.890	.874	.907	.894	.618	.337	.480	.378
2.51	.960	.952	.941	.929	.889	.873	.907	.891	.617	.371	.462	.335
3.00	.960	.951	.941	.929	.888	.873	.907	.886	.615	.256	.462	.334
4.02	.959	.949	.939	.927	.886	.872	.906	.881	.615	.251	.459	.332
5.01	.958	.948	.938	.926	.884	.872	.905	.874	.615	.247	.457	.331
6.00	.957	.947	.937	.925	.883	.871	.904	.857	.615	.244	.456	.332
7.00	.956	.946	.936	.923	.882	.870	.902	.854	.615	.236	.454	.326
8.00	.954	.944	.934	.922	.880	.869	.900	.853	.614	.233	.453	.324

Table 2. Nozzle Internal Static-Pressure Ratios

$[\delta_v = 0^\circ, \text{ maximum area configuration}]$

(a) Upper flap centerline

	x/l_{uf}											
NPR	-0.29	-0.18	-0.08	0.07	0.18	0.28	0.38	0.48	0.59	0.69	0.79	0.89
1.51	0.878	0.888	0.876	0.757	0.698	0.495	0.570	0.584	0.604	0.622	0.636	0.649
1.75	.874	.883	.871	.745	.684	.443	.499	.502	.512	.526	.538	.550
2.00	.873	.883	.870	.744	.682	.325	.432	.436	.445	.457	.471	.483
2.26	.873	.882	.869	.744	.682	.281	.205	.331	.385	.427	.452	.457
2.50	.873	.882	.869	.744	.682	.280	.168	.190	.332	.383	.431	.446
3.00	.873	.882	.869	.744	.681	.279	.168	.189	.202	.209	.343	.356
4.00	.871	.881	.867	.739	.676	.275	.165	.184	.196	.200	.200	.230
5.00	.869	.881	.867	.736	.674	.274	.163	.181	.194	.197	.196	.199

(b) Lower fixed flap centerline

	x'/l_{ls}		
NPR	0.32	0.56	0.78
1.51	0.877	0.882	0.897
1.75	.872	.878	.894
2.00	.871	.877	.893
2.26	.871	.877	.893
2.50	.870	.877	.893
3.00	.870	.876	.893
4.00	.868	.874	.892
5.00	.867	.873	.892

(c) Top surface centerline of lower rotating flap

	x''/l_{rf}							
NPR	0.05	0.18	0.30	0.42	0.54	0.67	0.79	0.92
1.51	0.900	0.864	0.815	0.671	0.673	0.672	0.646	0.638
1.75	.898	.859	.807	.651	.646	.635	.582	.536
2.00	.898	.859	.806	.648	.641	.628	.566	.504
2.26	.898	.859	.806	.648	.640	.627	.566	.500
2.50	.898	.859	.806	.648	.639	.627	.565	.500
3.00	.898	.859	.805	.648	.638	.626	.564	.500
4.00	.898	.857	.803	.642	.634	.624	.561	.498
5.00	.897	.856	.801	.639	.631	.622	.559	.497

Table 2. Concluded

(d) Right sidewall

NPR	pr_{sw2}	pr_{sw4}	pr_{sw5}	pr_{sw6}	pr_{sw7}	pr_{sw8}	pr_{sw9}	pr_{sw10}	pr_{sw11}	pr_{sw12}	pr_{sw17}	pr_{sw18}	pr_{sw19}
1.51	0.854	0.867	0.850	0.882	0.870	0.837	0.892	0.877	0.856	0.830	0.846	0.819	0.767
1.75	.849	.863	.844	.879	.866	.830	.889	.872	.850	.823	.840	.812	.757
2.00	.848	.862	.844	.878	.865	.830	.888	.871	.849	.823	.840	.812	.754
2.26	.849	.863	.845	.878	.866	.830	.888	.872	.850	.824	.841	.813	.758
2.50	.849	.863	.845	.879	.865	.830	.887	.872	.850	.823	.842	.813	.756
3.00	.849	.863	.845	.878	.865	.829	.886	.871	.849	.823	.842	.813	.758
4.00	.846	.861	.843	.876	.863	.826	.885	.869	.846	.821	.840	.810	.757
5.00	.844	.859	.842	.875	.862	.825	.883	.867	.844	.819	.839	.808	.756

NPR	pr_{sw20}	pr_{sw21}	pr_{sw22}	pr_{sw23}	pr_{sw25}	pr_{sw26}	pr_{sw27}	pr_{sw28}	pr_{sw29}	pr_{sw31}	pr_{sw32}	pr_{sw33}	pr_{sw34}
1.51	0.815	0.771	0.776	0.755	0.705	0.683	0.721	0.701	0.668	0.604	0.601	0.625	0.632
1.75	.807	.760	.764	.741	.684	.657	.703	.677	.629	.542	.492	.552	.529
2.00	.807	.759	.762	.739	.681	.654	.700	.674	.621	.429	.406	.522	.452
2.26	.808	.759	.762	.739	.680	.654	.700	.674	.620	.426	.309	.522	.447
2.50	.808	.759	.761	.739	.680	.653	.699	.674	.619	.427	.307	.521	.446
3.00	.808	.759	.760	.738	.679	.653	.699	.674	.618	.427	.306	.521	.444
4.00	.806	.755	.754	.733	.675	.650	.694	.670	.615	.431	.310	.521	.444
5.00	.804	.753	.752	.731	.672	.649	.692	.668	.614	.431	.310	.520	.442

NPR	pr_{sw35}	pr_{sw36}	pr_{sw37}
1.51	0.655	0.645	0.640
1.75	.562	.577	.542
2.00	.447	.560	.492
2.26	.375	.559	.490
2.50	.375	.559	.489
3.00	.374	.558	.488
4.00	.375	.556	.486
5.00	.374	.555	.484

Table 3. Nozzle Internal Static-Pressure Ratios

$[\delta_v = 60^\circ, \text{ minimum area configuration}]$

(a) Upper flap centerline

	x/l_{uf}											
NPR	-0.24	-0.15	-0.07	0.10	0.21	0.31	0.42	0.53	0.64	0.74	0.85	0.96
1.50	.981	.978	.975	.987	.990	.993	.907	.817	.404	.555	.661	.691
1.76	.980	.976	.973	.985	.988	.992	.907	.816	.405	.419	.499	.578
2.01	.979	.976	.972	.985	.988	.992	.906	.815	.405	.370	.415	.479
2.25	.980	.976	.972	.985	.988	.992	.907	.815	.406	.215	.353	.415
2.51	.979	.975	.971	.985	.987	.991	.906	.813	.405	.201	.389	.403
3.01	.979	.976	.972	.985	.987	.992	.905	.813	.405	.201	.240	.353
4.01	.978	.976	.972	.985	.988	.992	.904	.811	.405	.200	.140	.235
5.01	.977	.976	.972	.986	.989	.993	.902	.811	.405	.200	.139	.159
6.02	.976	.976	.972	.984	.988	.992	.901	.809	.405	.200	.138	.097
6.62	.976	.976	.973	.983	.987	.991	.900	.807	.405	.200	.138	.097

(b) Lower fixed flap centerline

	x'/l_{ls}		
NPR	0.32	0.56	0.78
1.50	0.903	0.825	0.517
1.76	.895	.812	.416
2.01	.893	.809	.405
2.25	.893	.809	.403
2.51	.892	.809	.396
3.01	.892	.809	.399
4.01	.892	.809	.398
5.01	.891	.808	.389
6.02	.891	.808	.393
6.62	.891	.807	.391

Table 3. Continued

(c) Forward surface centerline of lower rotating flap

	x''/l_{rf}							
NPR	0.05	0.18	0.30	0.43	0.55	0.68	0.80	0.93
1.50	0.918	0.867	0.768	0.635	0.666	0.669	0.672	0.681
1.76	.905	.848	.728	.428	.577	.573	.573	.582
2.01	.903	.845	.720	.406	.410	.561	.511	.494
2.25	.902	.845	.718	.399	.379	.330	.514	.504
2.51	.901	.845	.718	.400	.352	.296	.281	.433
3.01	.902	.845	.718	.402	.352	.251	.219	.183
4.01	.902	.844	.717	.400	.351	.248	.181	.133
5.01	.904	.844	.715	.399	.350	.248	.177	.123
6.02	.903	.843	.714	.398	.350	.248	.172	.123
6.62	.903	.842	.713	.398	.350	.248	.171	.123

(d) Aft surface centerline of lower rotating flap

	x''/l_{rf}							
NPR	0.05	0.18	0.30	0.42	0.54	0.67	0.79	0.92
1.50	0.955	0.958	0.896	0.658	0.375	0.547	0.648	0.691
1.76	.954	.957	.897	.658	.319	.428	.501	.572
2.01	.953	.957	.898	.658	.320	.297	.407	.473
2.25	.954	.957	.900	.658	.321	.198	.372	.417
2.51	.953	.957	.896	.657	.321	.202	.337	.373
3.01	.953	.957	.894	.657	.320	.197	.275	.288
4.01	.952	.956	.890	.657	.320	.196	.136	.144
5.01	.951	.956	.889	.655	.319	.195	.137	.103
6.02	.950	.955	.888	.653	.319	.195	.137	.103
6.62	.948	.954	.887	.652	.319	.194	.137	.103

Table 3. Concluded

(e) Right sidewall

NPR	pr_{sw2}	pr_{sw4}	pr_{sw5}	pr_{sw6}	pr_{sw7}	pr_{sw8}	pr_{sw9}	pr_{sw10}	pr_{sw11}	pr_{sw12}	pr_{sw13}	pr_{sw16}	pr_{sw17}
1.50	0.956	0.930	0.928	0.881	0.902	0.878	0.749	0.786	0.784	0.826	0.652	0.707	0.981
1.76	.953	.924	.920	.870	.892	.863	.710	.753	.753	.800	.563	.649	.980
2.01	.952	.922	.917	.868	.889	.859	.703	.746	.745	.794	.516	.639	.980
2.25	.953	.922	.919	.868	.889	.859	.702	.745	.744	.794	.500	.638	.980
2.51	.953	.921	.919	.868	.888	.859	.702	.744	.744	.793	.490	.637	.979
3.01	.953	.921	.919	.868	.888	.859	.703	.745	.743	.793	.482	.636	.979
4.01	.951	.920	.918	.868	.887	.860	.702	.744	.741	.793	.491	.636	.979
5.01	.949	.919	.915	.867	.886	.860	.702	.743	.739	.793	.477	.636	.978
6.02	.950	.919	.916	.865	.886	.859	.701	.743	.740	.792	.468	.637	.977
6.62	.949	.918	.917	.864	.886	.859	.700	.742	.740	.791	.475	.635	.976

NPR	pr_{sw18}	pr_{sw19}	pr_{sw20}	pr_{sw21}	pr_{sw22}	pr_{sw23}
1.50	0.981	0.983	0.981	0.988	0.974	0.982
1.76	.980	.983	.981	.989	.974	.982
2.01	.980	.984	.981	.989	.975	.983
2.25	.980	.985	.981	.989	.974	.982
2.51	.980	.984	.980	.989	.974	.982
3.01	.980	.983	.980	.988	.974	.981
4.01	.979	.984	.979	.987	.972	.980
5.01	.977	.984	.978	.987	.972	.979
6.02	.977	.982	.977	.985	.970	.978
6.62	.976	.982	.977	.985	.969	.977

Table 4. Nozzle Internal Static-Pressure Ratios

$[\delta_v = 60^\circ, \text{maximum area configuration}]$

(a) Upper flap centerline

	x/l_{uf}													
NPR	-0.25	-0.16	-0.07	0.06	0.15	0.24	0.33	0.42	0.51	0.60	0.69	0.78	0.87	0.97
1.50	0.940	0.944	0.949	0.953	0.958	0.938	0.863	0.707	0.649	0.528	0.608	0.662	0.678	0.677
1.76	.937	.941	.945	.950	.956	.937	.863	.708	.649	.527	.385	.498	.575	.596
2.00	.936	.941	.944	.950	.956	.937	.864	.709	.650	.526	.385	.273	.442	.488
2.25	.936	.940	.944	.950	.956	.937	.864	.709	.650	.526	.385	.270	.381	.415
2.50	.936	.940	.943	.950	.956	.936	.864	.709	.650	.526	.384	.270	.223	.370
3.00	.935	.940	.943	.949	.956	.936	.864	.709	.650	.525	.384	.269	.221	.212
4.00	.934	.940	.944	.949	.956	.936	.863	.707	.649	.524	.383	.268	.217	.208
4.71	.934	.940	.944	.949	.956	.935	.861	.703	.646	.523	.382	.268	.215	.207

(b) Lower fixed flap centerline

	x'/l_{ls}		
NPR	0.32	0.56	0.78
1.50	0.843	0.763	0.471
1.76	.831	.745	.365
2.00	.828	.742	.346
2.25	.827	.741	.341
2.50	.826	.741	.341
3.00	.825	.740	.340
4.00	.825	.740	.338
4.71	.825	.740	.338

(c) Forward surface centerline of lower rotating flap

	x''/l_{rf}							
NPR	0.05	0.18	0.30	0.43	0.55	0.68	0.80	0.93
1.50	0.968	0.888	0.776	0.638	0.666	0.669	0.672	0.689
1.76	.957	.867	.732	.431	.574	.573	.574	.595
2.00	.955	.862	.720	.402	.404	.561	.511	.503
2.25	.954	.861	.716	.393	.373	.326	.520	.493
2.50	.954	.861	.717	.394	.345	.291	.278	.455
3.00	.953	.861	.716	.394	.345	.247	.217	.311
4.00	.953	.861	.716	.393	.344	.246	.181	.131
4.71	.953	.860	.715	.391	.344	.246	.178	.124

Table 4. Concluded

(d) Aft surface centerline of lower rotating flap

$$x''/l_{\text{rf}}$$

NPR	0.05	0.18	0.30	0.42	0.54	0.67	0.79	0.92
1.50	0.613	0.762	0.723	0.494	0.466	0.650	0.681	0.707
1.76	.611	.767	.722	.493	.324	.485	.574	.627
2.00	.611	.769	.721	.492	.324	.308	.482	.532
2.25	.613	.771	.722	.492	.324	.307	.351	.463
2.50	.614	.772	.721	.491	.323	.306	.273	.436
3.00	.617	.772	.721	.491	.322	.304	.273	.227
4.00	.620	.772	.720	.491	.319	.301	.272	.226
4.71	.626	.771	.719	.491	.319	.300	.272	.226

(e) Right sidewall

NPR	$pr_{\text{sw}2}$	$pr_{\text{sw}4}$	$pr_{\text{sw}5}$	$pr_{\text{sw}6}$	$pr_{\text{sw}7}$	$pr_{\text{sw}8}$	$pr_{\text{sw}9}$	$pr_{\text{sw}10}$	$pr_{\text{sw}11}$	$pr_{\text{sw}12}$	$pr_{\text{sw}13}$	$pr_{\text{sw}16}$	$pr_{\text{sw}17}$
1.50	0.923	0.897	0.934	0.821	0.880	0.894	0.718	0.780	0.804	0.834	0.659	0.714	0.943
1.76	.919	.887	.928	.804	.866	.877	.667	.740	.770	.803	.570	.650	.941
2.00	.918	.885	.927	.800	.863	.873	.652	.728	.760	.795	.516	.636	.941
2.25	.918	.885	.928	.800	.863	.872	.649	.725	.757	.793	.488	.631	.941
2.50	.919	.885	.929	.799	.863	.874	.649	.725	.756	.793	.459	.631	.941
3.00	.918	.885	.929	.799	.863	.875	.648	.725	.756	.793	.440	.629	.940
4.00	.918	.885	.929	.798	.863	.875	.647	.724	.755	.792	.469	.628	.939
4.71	.917	.884	.929	.797	.862	.876	.646	.723	.755	.792	.462	.628	.939

NPR	$pr_{\text{sw}18}$	$pr_{\text{sw}19}$	$pr_{\text{sw}20}$	$pr_{\text{sw}21}$	$pr_{\text{sw}22}$	$pr_{\text{sw}23}$	$pr_{\text{sw}25}$	$pr_{\text{sw}27}$	$pr_{\text{sw}28}$
1.50	0.919	0.948	0.845	0.894	0.795	0.790	0.867	0.755	0.757
1.76	.916	.947	.846	.893	.796	.788	.867	.754	.758
2.00	.916	.948	.848	.893	.798	.789	.867	.754	.759
2.25	.916	.948	.848	.893	.798	.789	.868	.754	.760
2.50	.916	.948	.848	.893	.798	.789	.867	.754	.760
3.00	.916	.948	.843	.892	.798	.789	.867	.753	.761
4.00	.915	.948	.847	.891	.795	.786	.865	.752	.759
4.71	.915	.947	.844	.889	.793	.784	.862	.750	.753

Table 5. Nozzle Internal Static-Pressure Ratios

$[\delta_v = 105^\circ, \text{ minimum area configuration}]$

(a) Upper flap centerline

	x/l_{uf}						
NPR	-0.24	-0.16	-0.07	0.09	0.18	0.27	0.35
1.50	0.994	0.993	0.991	0.998	0.998	1.001	1.000
1.75	.993	.991	.989	.997	.998	1.000	.999
2.02	.992	.990	.987	.996	.997	1.000	1.000
2.25	.992	.990	.987	.996	.998	1.000	1.000
2.52	.992	.990	.987	.997	.997	1.000	1.000
3.02	.991	.989	.986	.996	.997	.999	1.000
4.02	.990	.989	.987	.995	.997	.999	1.001
5.02	.989	.989	.987	.995	.997	.999	1.001
5.98	.989	.990	.987	.994	.997	.998	1.001
7.02	.989	.990	.988	.993	.997	.997	1.000
8.00	.989	.990	.988	.992	.997	.997	.998

(b) Lower fixed flap centerline

	x'/l_{ls}	
NPR	0.32	0.56
1.50	0.966	0.936
1.75	.960	.926
2.02	.956	.919
2.25	.954	.916
2.52	.953	.913
3.02	.952	.911
4.02	.951	.909
5.02	.951	.908
5.98	.951	.907
7.02	.950	.905
8.00	.949	.904

Table 5. Concluded

(c) Forward surface centerline of lower rotating flap

	x''/l_{rf}							
NPR	0.05	0.18	0.30	0.43	0.55	0.68	0.80	0.93
1.50	1.003	1.001	0.990	0.954	0.898	0.812	0.723	0.676
1.75	1.002	1.001	.987	.944	.876	.763	.641	.579
2.02	1.001	1.001	.986	.937	.861	.728	.574	.508
2.25	1.001	1.001	.985	.934	.854	.708	.535	.440
2.52	1.001	1.001	.985	.932	.848	.692	.501	.387
3.02	1.000	1.001	.984	.929	.842	.673	.464	.333
4.02	.999	1.000	.982	.927	.836	.655	.430	.288
5.02	.999	.999	.981	.925	.833	.644	.408	.273
5.98	.999	.998	.978	.924	.832	.640	.395	.258
7.02	.999	.996	.976	.922	.831	.638	.390	.247
8.00	.999	.994	.973	.920	.830	.637	.390	.243

(d) Right sidewall

NPR	$pr_{\text{sw}2}$	$pr_{\text{sw}4}$	$pr_{\text{sw}5}$	$pr_{\text{sw}6}$	$pr_{\text{sw}7}$	$pr_{\text{sw}8}$	$pr_{\text{sw}9}$	$pr_{\text{sw}10}$	$pr_{\text{sw}11}$	$pr_{\text{sw}12}$	$pr_{\text{sw}13}$	$pr_{\text{sw}16}$	$pr_{\text{sw}17}$
1.50	0.984	0.981	0.978	0.970	0.975	0.965	0.927	0.934	0.934	0.956	0.726	0.929	0.994
1.75	.982	.978	.975	.966	.971	.959	.915	.924	.922	.948	.680	.915	.993
2.02	.980	.976	.973	.963	.968	.955	.908	.918	.915	.943	.657	.906	.993
2.25	.980	.976	.972	.962	.968	.954	.905	.915	.913	.942	.652	.902	.993
2.52	.979	.975	.971	.961	.967	.952	.903	.913	.910	.940	.648	.899	.992
3.02	.979	.974	.971	.960	.966	.951	.901	.912	.909	.939	.647	.897	.992
4.02	.977	.972	.969	.959	.964	.949	.899	.909	.906	.938	.667	.894	.990
5.02	.976	.972	.968	.958	.963	.948	.898	.908	.904	.936	.676	.893	.990
5.98	.975	.971	.967	.956	.963	.948	.897	.907	.903	.935	.683	.891	.989
7.02	.973	.970	.966	.954	.961	.947	.895	.905	.902	.934	.683	.889	.988
8.00	.973	.969	.965	.952	.960	.945	.893	.904	.901	.932	.680	.887	.987

NPR	$pr_{\text{sw}18}$	$pr_{\text{sw}19}$	$pr_{\text{sw}20}$	$pr_{\text{sw}21}$	$pr_{\text{sw}22}$
1.50	0.992	0.993	0.990	0.997	0.996
1.75	.991	.995	.989	.997	.996
2.02	.990	.994	.987	.997	.995
2.25	.990	.995	.987	.997	.995
2.52	.990	.995	.987	.997	.995
3.02	.989	.995	.986	.997	.994
4.02	.988	.995	.985	.996	.994
5.02	.987	.994	.984	.995	.992
5.98	.986	.993	.983	.994	.992
7.02	.985	.992	.982	.993	.990
8.00	.984	.991	.981	.991	.989

Table 6. Nozzle Internal Static-Pressure Ratios

$[\delta_v = 105^\circ, \text{maximum area configuration}]$

(a) Upper flap centerline

	x/l_{uf}											
NPR	-0.28	-0.18	-0.08	0.10	0.20	0.30	0.40	0.51	0.61	0.71	0.81	0.91
1.51	0.977	0.977	0.977	0.969	0.949	0.962	0.929	0.686	0.421	0.582	0.608	0.629
1.76	.975	.974	.975	.966	.946	.958	.922	.643	.317	.462	.479	.512
2.01	.974	.974	.974	.966	.946	.958	.922	.643	.316	.443	.445	.461
2.26	.973	.973	.973	.966	.945	.957	.922	.643	.316	.401	.403	.413
2.51	.973	.973	.973	.966	.945	.957	.922	.642	.316	.365	.367	.374
3.00	.972	.972	.973	.966	.946	.957	.923	.642	.316	.155	.166	.188
4.00	.971	.972	.973	.967	.946	.956	.924	.642	.316	.155	.169	.185
5.02	.970	.972	.974	.966	.946	.955	.923	.643	.316	.154	.171	.185
5.82	.969	.972	.974	.966	.946	.955	.923	.643	.315	.153	.171	.184

(b) Lower fixed flap centerline

	x'/l_s	
NPR	0.32	0.56
1.51	0.934	0.897
1.76	.925	.884
2.01	.922	.877
2.26	.919	.873
2.51	.917	.870
3.00	.915	.866
4.00	.914	.863
5.02	.913	.862
5.82	.913	.861

(c) Forward surface centerline of lower rotating flap

	x''/l_{rf}							
NPR	0.05	0.18	0.30	0.43	0.55	0.68	0.80	0.93
1.51	0.953	1.001	0.995	0.959	0.902	0.808	0.716	0.666
1.76	.953	1.002	.993	.950	.882	.763	.641	.588
2.01	.954	1.004	.993	.945	.868	.732	.581	.512
2.26	.955	1.004	.992	.942	.859	.710	.538	.444
2.51	.956	1.005	.992	.940	.854	.695	.509	.398
3.00	.956	1.005	.992	.937	.847	.674	.466	.335
4.00	.956	1.003	.990	.933	.840	.656	.432	.291
5.02	.956	1.002	.988	.932	.837	.645	.413	.275
5.82	.957	1.002	.987	.932	.836	.641	.400	.264

Table 6. Concluded

(d) Aft surface centerline of lower rotating flap

$$x''/l_{\text{rf}}$$

NPR	0.05	0.18	0.30	0.42	0.54	0.67	0.79	0.92
1.51	0.377	0.453	0.553	0.603	0.621	0.631	0.642	0.649
1.76	.112	.320	.527	.357	.498	.557	.573	.593
2.01	.108	.317	.509	.340	.392	.481	.511	.532
2.26	.105	.317	.409	.337	.344	.388	.439	.480
2.51	.101	.317	.252	.343	.238	.352	.398	.437
3.00	.096	.317	.252	.259	.281	.282	.289	.303
4.00	.090	.318	.252	.134	.201	.194	.202	.214
5.02	.086	.317	.252	.134	.145	.137	.142	.153
5.82	.084	.317	.252	.134	.117	.111	.117	.128

(e) Right sidewall

NPR	$pr_{\text{sw}2}$	$pr_{\text{sw}4}$	$pr_{\text{sw}5}$	$pr_{\text{sw}6}$	$pr_{\text{sw}7}$	$pr_{\text{sw}8}$	$pr_{\text{sw}9}$	$pr_{\text{sw}10}$	$pr_{\text{sw}11}$	$pr_{\text{sw}12}$	$pr_{\text{sw}13}$	$pr_{\text{sw}16}$	$pr_{\text{sw}17}$
1.51	0.972	0.961	0.973	0.929	0.958	0.972	0.892	0.924	0.940	0.960	0.693	0.944	0.976
1.76	.969	.957	.970	.920	.953	.968	.875	.913	.931	.953	.639	.932	.974
2.01	.969	.955	.970	.916	.951	.966	.867	.908	.927	.950	.611	.926	.974
2.26	.968	.954	.969	.914	.948	.965	.863	.904	.923	.948	.601	.921	.974
2.51	.968	.953	.969	.913	.948	.964	.861	.903	.921	.948	.597	.919	.974
3.00	.967	.952	.968	.911	.946	.963	.858	.900	.918	.946	.597	.916	.973
4.00	.965	.950	.967	.909	.944	.961	.854	.897	.916	.944	.617	.914	.971
5.02	.964	.949	.966	.907	.943	.961	.853	.896	.916	.942	.632	.913	.970
5.82	.964	.949	.966	.906	.943	.961	.852	.895	.916	.941	.639	.913	.970

NPR	$pr_{\text{sw}18}$	$pr_{\text{sw}19}$	$pr_{\text{sw}20}$	$pr_{\text{sw}21}$	$pr_{\text{sw}22}$	$pr_{\text{sw}23}$	$pr_{\text{sw}25}$	$pr_{\text{sw}28}$	$pr_{\text{sw}29}$
1.51	0.973	0.962	0.979	0.951	0.992	0.990	0.696	0.444	0.705
1.76	.971	.962	.978	.950	.993	.991	.680	.283	.676
2.01	.971	.963	.978	.950	.994	.993	.680	.281	.676
2.26	.971	.963	.978	.950	.995	.995	.674	.279	.676
2.51	.971	.963	.978	.951	.995	.995	.668	.278	.675
3.00	.970	.962	.977	.950	.994	.995	.670	.277	.676
4.00	.969	.962	.976	.949	.993	.994	.668	.274	.677
5.02	.968	.961	.975	.948	.992	.994	.677	.274	.679
5.82	.967	.960	.975	.948	.991	.993	.679	.275	.680

Table 7. Nozzle Internal Performance Characteristics

(a) $\delta_v = 0^\circ$, minimum area configuration

NPR	F_r/F_i	F_a/F_i	δ_p , deg	w_p/w_i
1.50	0.9154	0.9028	-9.49	0.9126
1.76	.9175	.9045	-9.66	.9198
2.00	.9295	.9066	-12.73	.9341
2.27	.9416	.9153	-13.57	.9421
2.51	.9500	.9313	-11.39	.9435
3.00	.9636	.9466	-10.77	.9454
4.02	.9729	.9468	-13.32	.9484
5.01	.9752	.9632	-8.98	.9529
6.00	.9763	.9709	-6.03	.9567
7.00	.9758	.9734	-4.04	.9604
8.00	.9755	.9744	-2.62	.9641

(b) $\delta_v = 0^\circ$, maximum area configuration

NPR	F_r/F_i	F_a/F_i	δ_p , deg	w_p/w_i
1.51	0.9374	0.9363	-2.75	0.9932
1.75	.9504	.9499	-1.79	.9731
2.00	.9604	.9591	-2.93	.9724
2.26	.9603	.9539	-6.58	.9735
2.50	.9649	.9566	-7.53	.9743
3.00	.9697	.9596	-8.29	.9754
4.00	.9732	.9657	-7.10	.9820
5.00	.9717	.9667	-5.79	.9839

(c) $\delta_v = 60^\circ$, minimum area configuration

NPR	F_r/F_i	F_a/F_i	δ_p , deg	w_p/w_i
1.50	0.9862	0.4960	59.81	0.9824
1.76	.9861	.5059	59.13	.9822
2.01	.9872	.5113	58.81	.9859
2.25	.9867	.5022	59.41	.9882
2.51	.9848	.5254	57.76	.9882
3.01	.9792	.5247	57.60	.9886
4.01	.9738	.4395	63.17	.9895
5.01	.9749	.3996	65.80	.9899
6.02	.9797	.3723	67.66	.9900
6.62	.9809	.3576	68.62	.9905

Table 7. Concluded

(d) $\delta_v = 60^\circ$, maximum area configuration

NPR	F_r/F_i	F_a/F_i	δ_p , deg	w_p/w_i
1.50	0.9943	0.4723	61.64	0.9892
1.76	.9889	.4767	61.18	.9760
2.00	.9879	.4816	60.82	.9785
2.25	.9892	.4756	61.26	.9807
2.50	.9876	.4974	59.76	.9807
3.00	.9856	.4803	60.83	.9810
4.00	.9905	.4441	63.36	.9823
4.71	.9947	.4159	65.29	.9814

(e) $\delta_v = 105^\circ$, minimum area configuration

NPR	F_r/F_i	F_a/F_i	δ_p , deg	w_p/w_i
1.50	0.9533	-0.1299	97.83	0.8342
1.76	.9574	-.1331	97.99	.8678
2.01	.9567	-.1383	98.31	.8964
2.25	.9574	-.1382	98.30	.9131
2.51	.9562	-.1502	99.04	.9238
3.01	.9477	-.1726	100.50	.9346
4.01	.9367	-.2253	103.92	.9434
5.03	.9297	-.2636	106.47	.9468
5.00	.9307	-.2637	106.46	.9469
6.00	.9238	-.2852	107.98	.9486
7.05	.9175	-.2992	109.03	.9506
7.02	.9189	-.2994	109.02	.9511
8.00	.9181	-.3102	109.75	.9526

(f) $\delta_v = 105^\circ$, maximum area configuration

NPR	F_r/F_i	F_a/F_i	δ_p , deg	w_p/w_i
1.51	0.8985	-0.1187	97.59	0.8774
1.76	.9064	-.1538	99.77	.8924
2.01	.9189	-.1725	100.82	.9088
2.26	.9280	-.1883	101.71	.9197
2.51	.9349	-.2012	102.43	.9266
3.01	.9143	-.1548	99.75	.9340
4.03	.9227	-.1900	101.89	.9399
5.00	.9340	-.2115	103.09	.9413

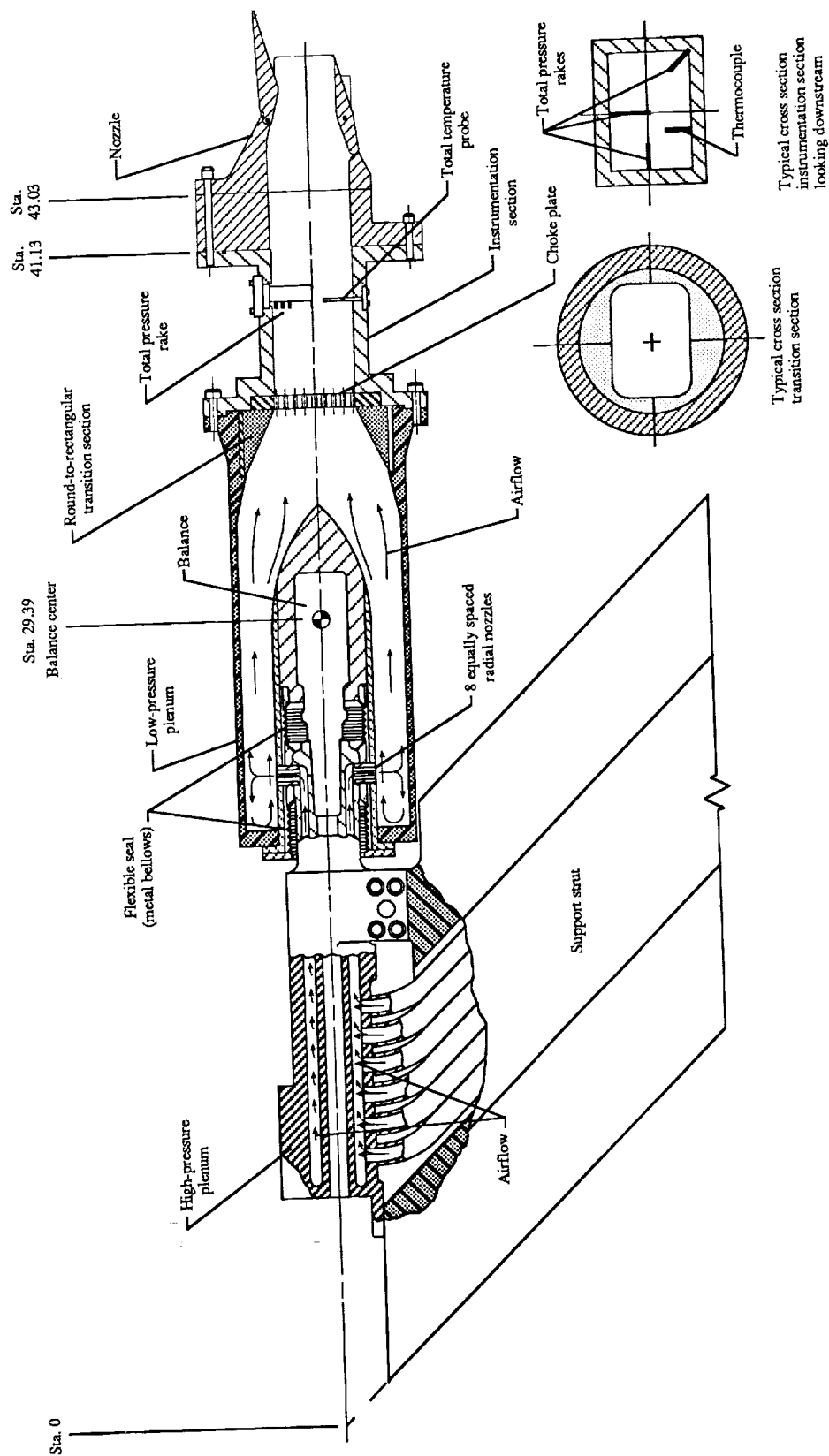
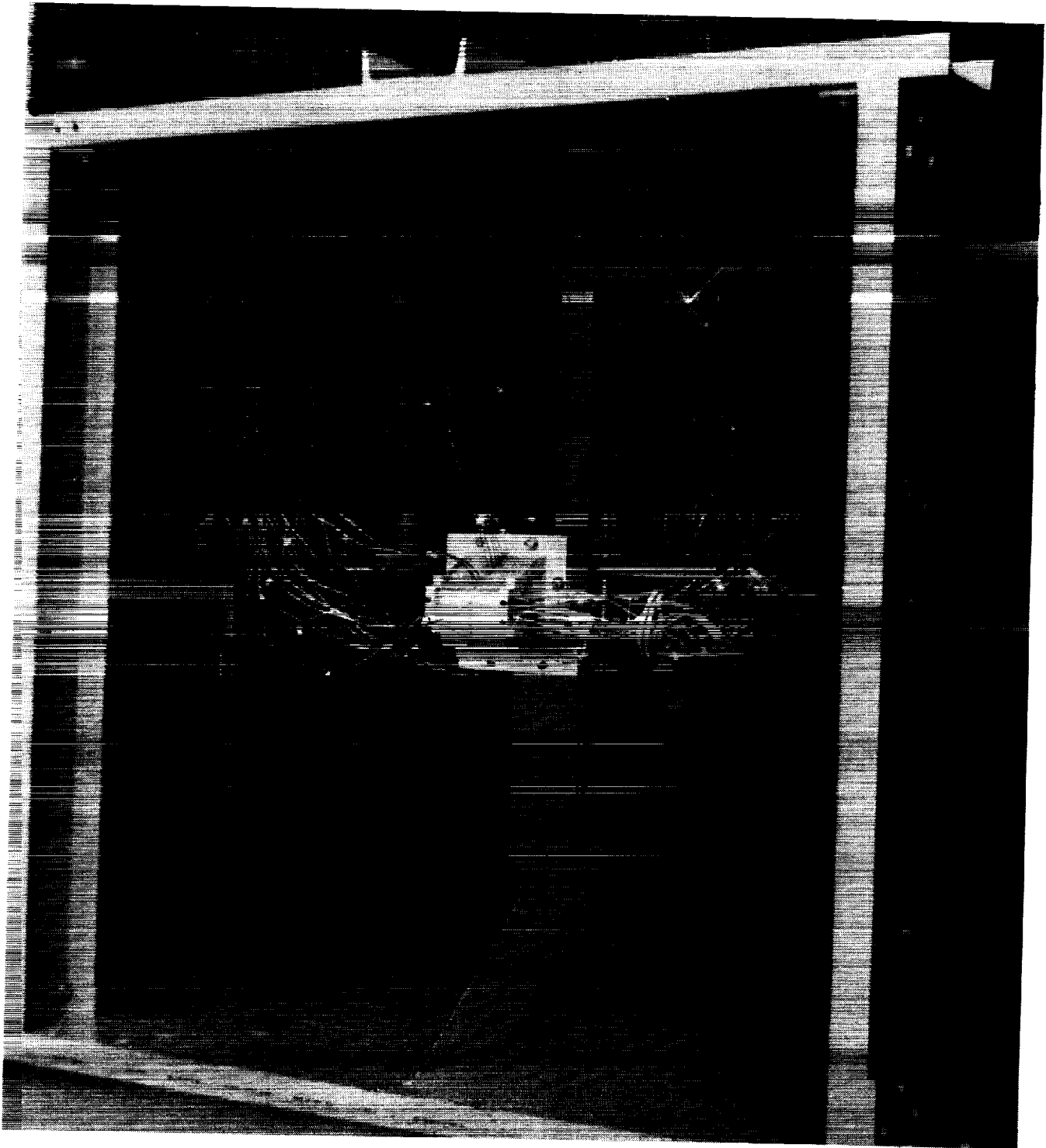


Figure 1. Sketch of single-engine propulsion simulator with typical nozzle. All linear dimensions are in inches.

ORIGINAL PAGE
BLACK AND WHITE PHOTOGRAPH

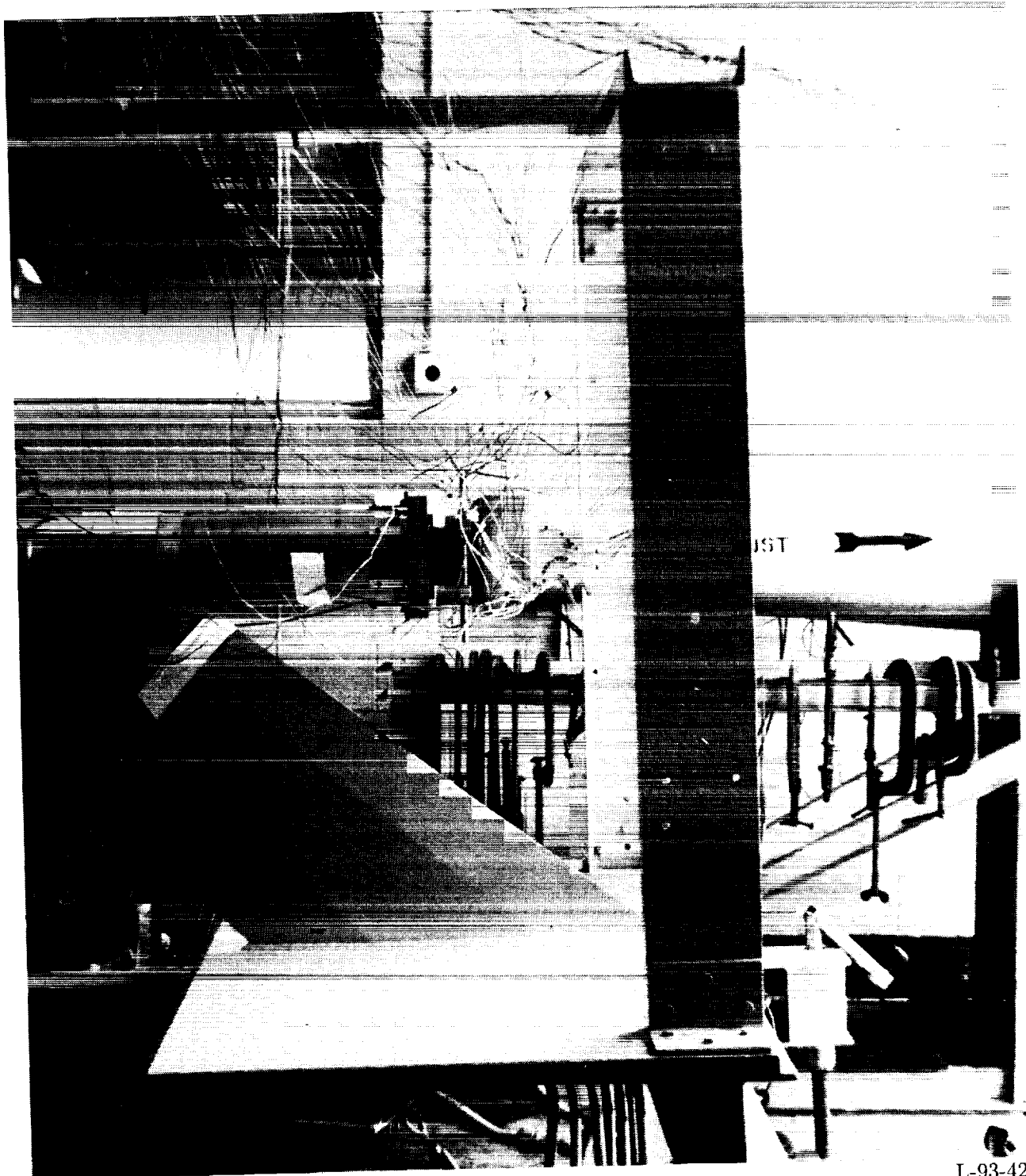


(a) Rear quarter view.

L-93-41

Figure 2. Photographs of typical nozzle on single-engine propulsion simulator.

ORIGINAL PAGE
BLACK AND WHITE PHOTOGRAPH



L-93-42

(b) Side view.

Figure 2. Concluded.

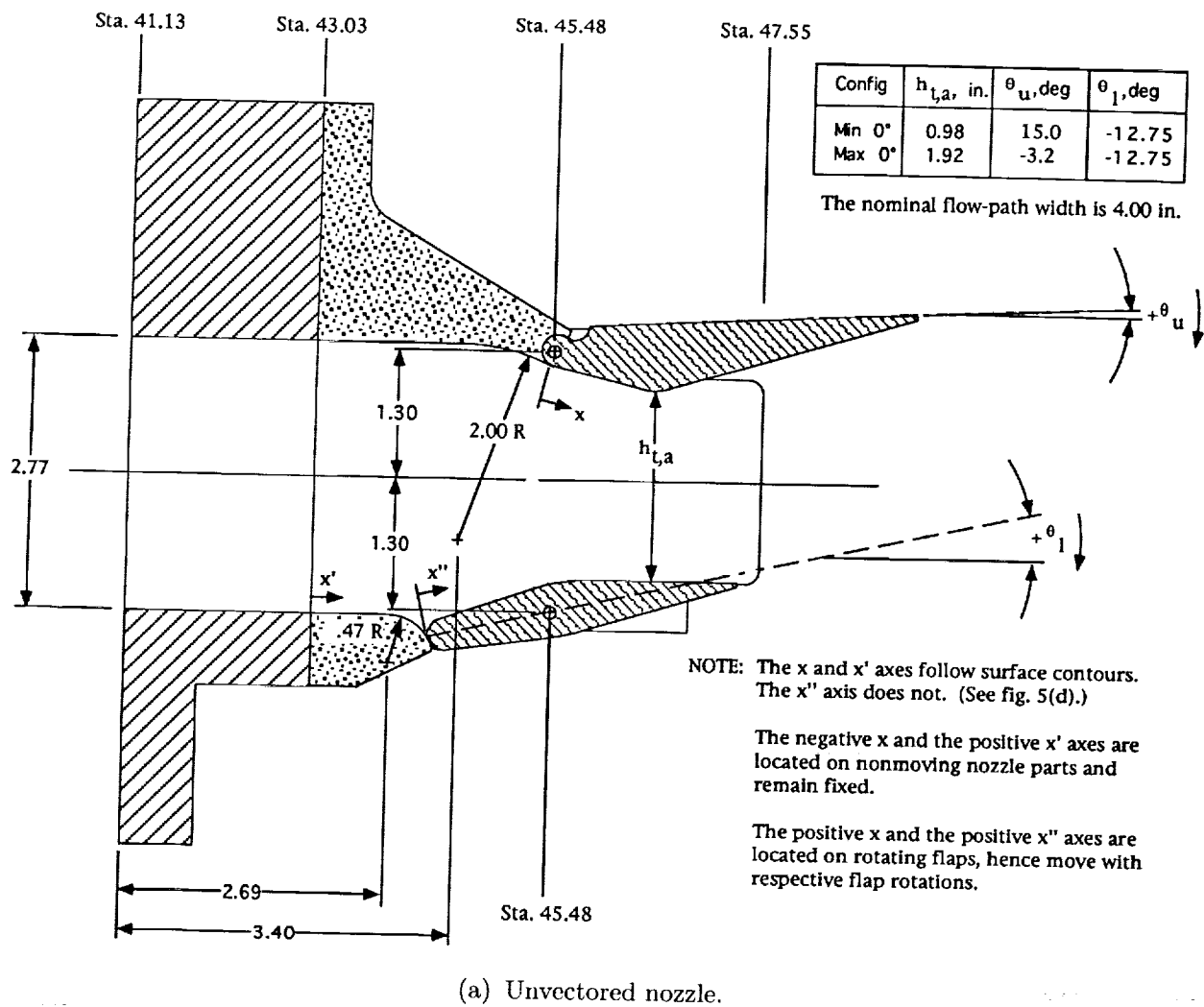
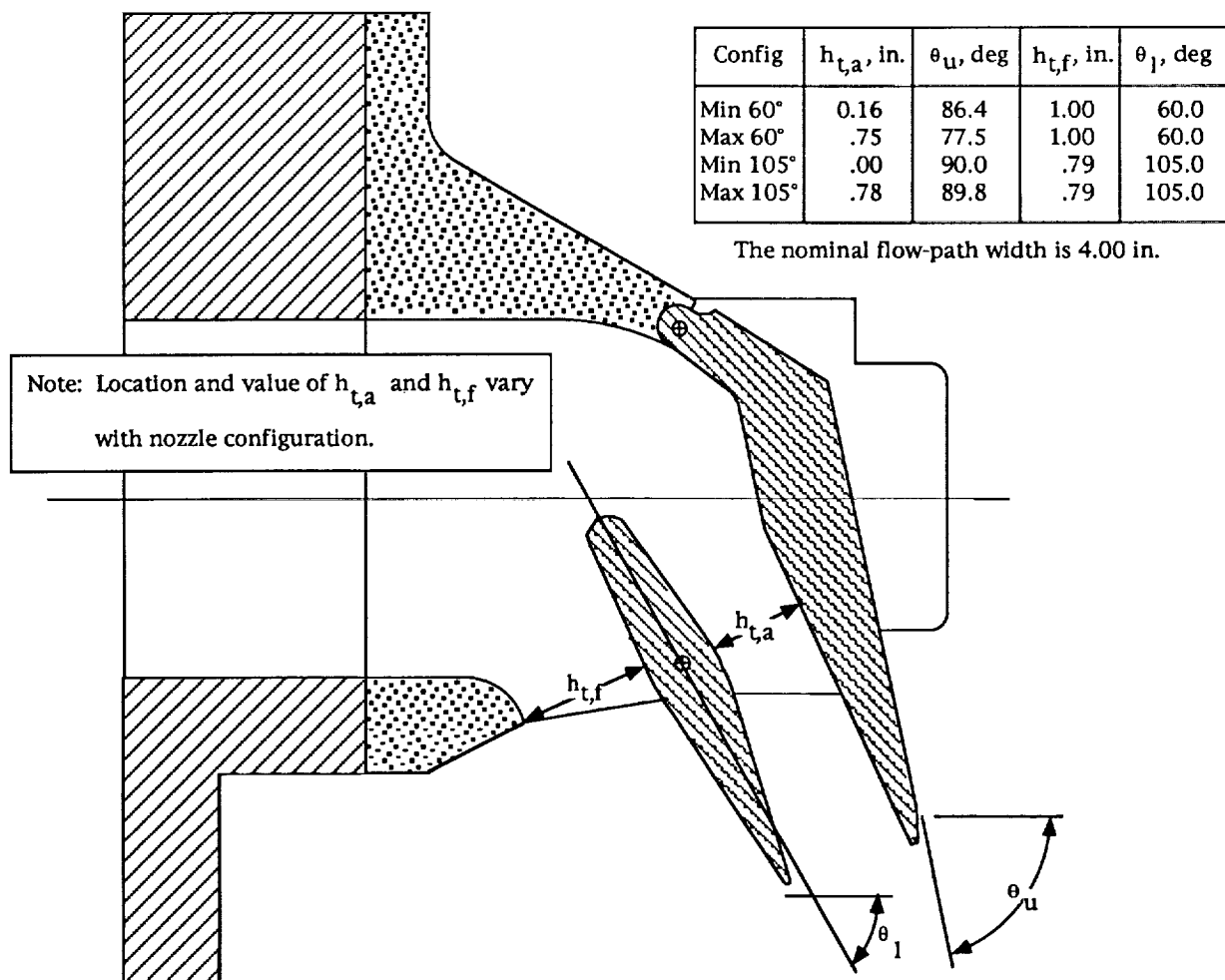
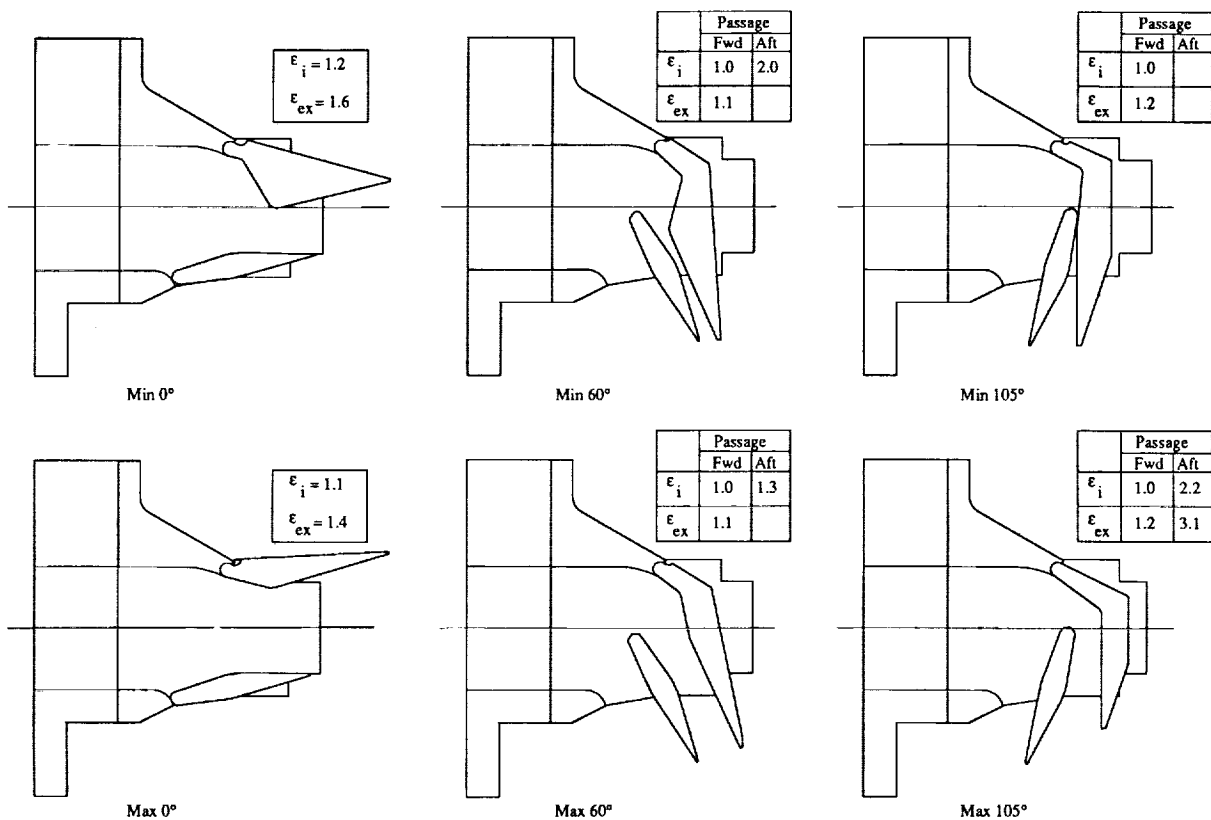


Figure 3. Sketches defining nozzle geometries, reference axes, and important nozzle parameters. All linear dimensions are in inches unless otherwise noted.



(b) Vectored nozzle.

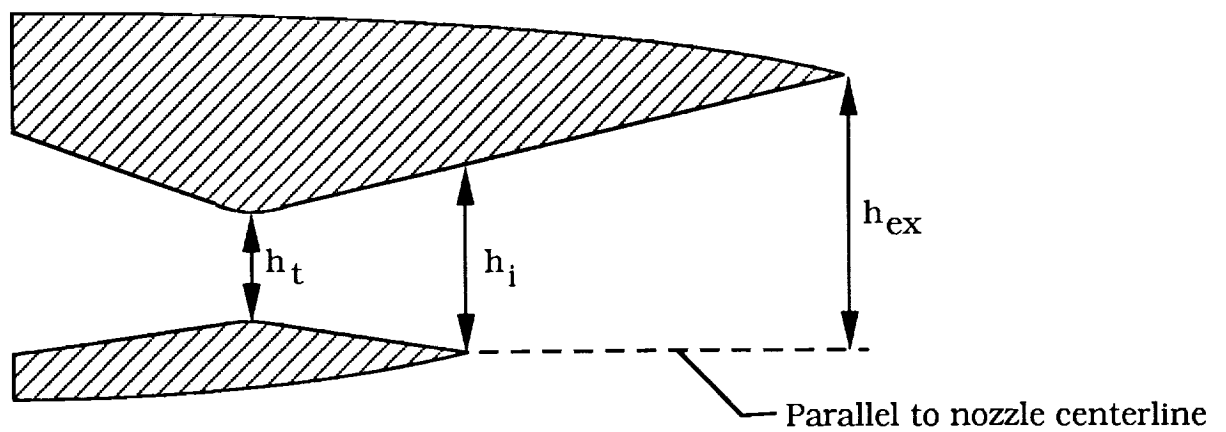
Figure 3. Continued.



(c) Sketches of test configurations, including estimated internal- and external-expansion ratios.

Figure 3. Continued.

Constant-width, single expansion-ramp nozzle



Internal-expansion ratio

$$\epsilon_i = h_i / h_t$$

External-expansion ratio

$$\epsilon_{ex} = h_{ex} / h_t$$

- (d) Definitions of internal- and external-expansion ratios for generic, constant-width, single expansion-ramp nozzle.

Figure 3. Concluded.

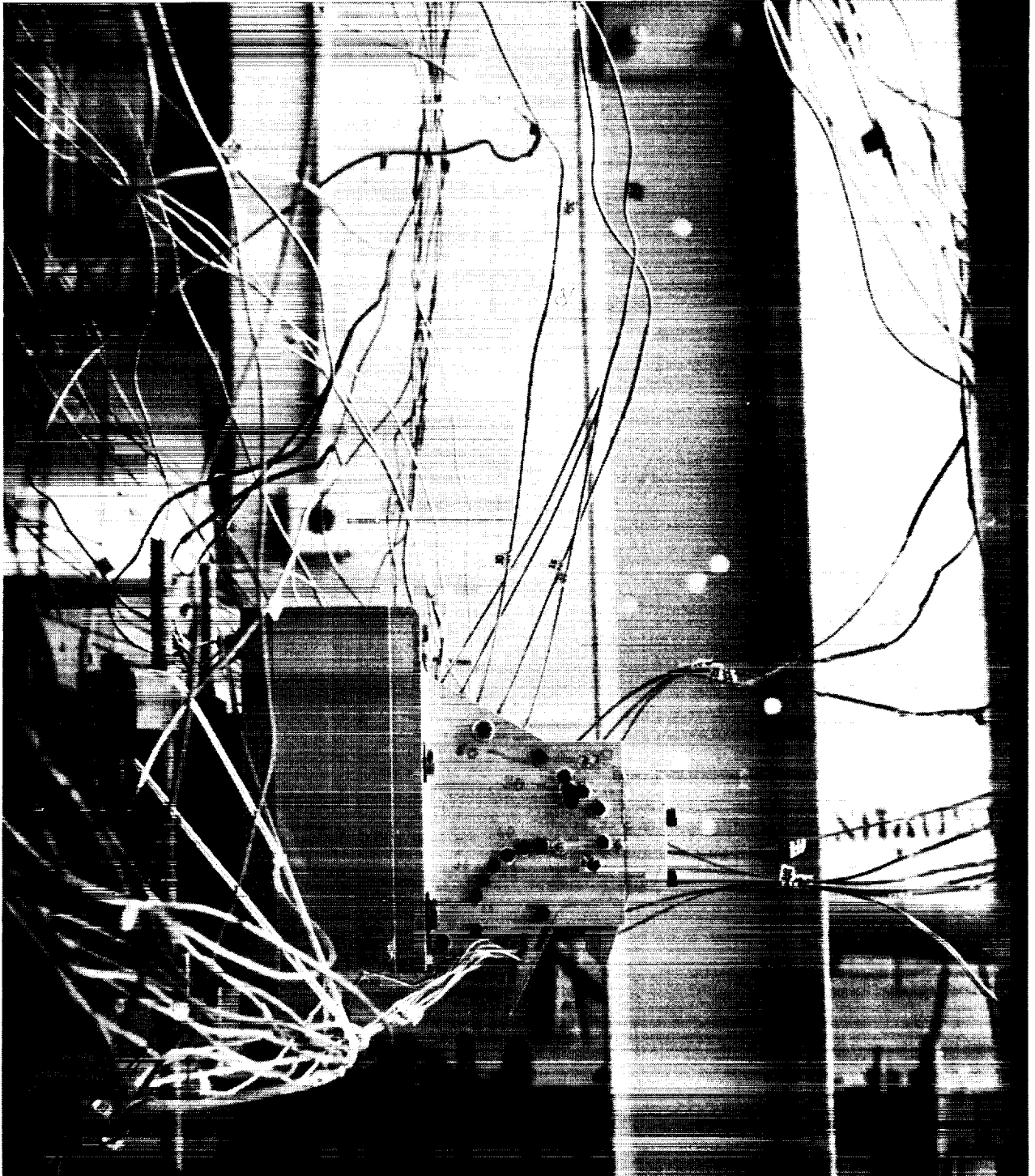


L-93-43

(a) $\delta_v = 60^\circ$, maximum area configuration, side view.

Figure 4. Photographs of vectored-nozzle configurations.

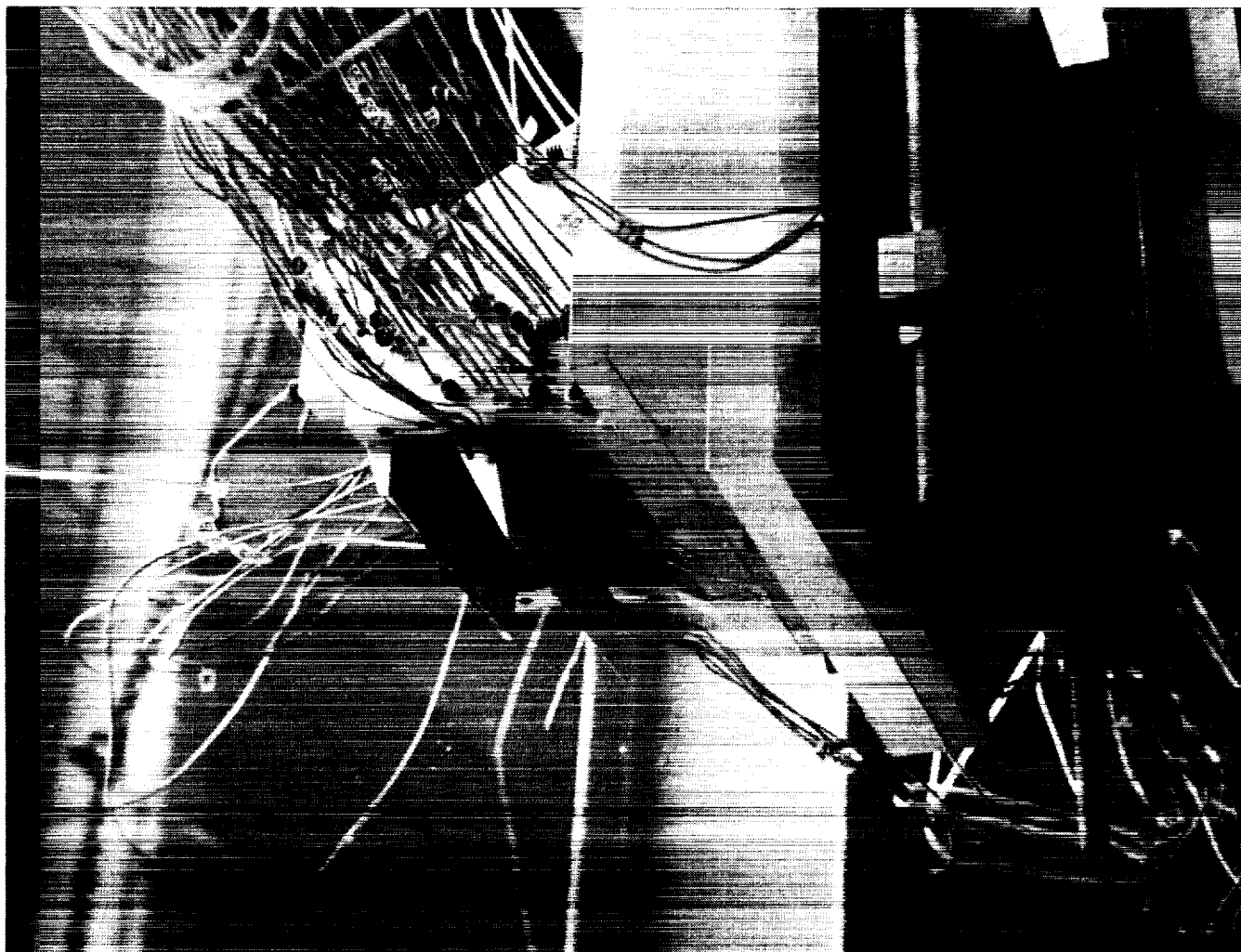
ORIGINAL PAGE
BLACK AND WHITE PHOTOGRAPH



(b) $\delta_v = 105^\circ$, maximum area configuration, side view.

L-93-44

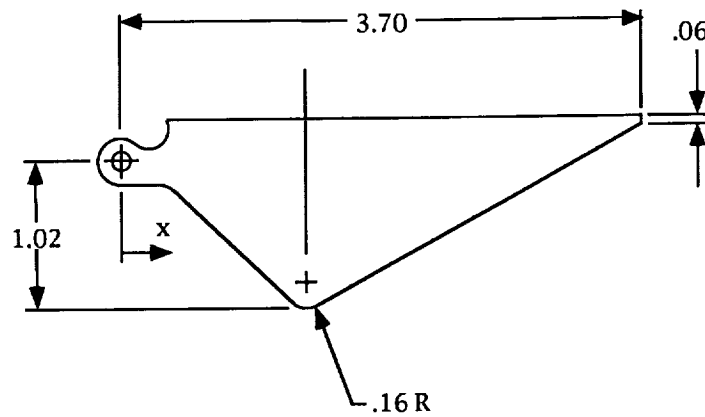
Figure 4. Continued.



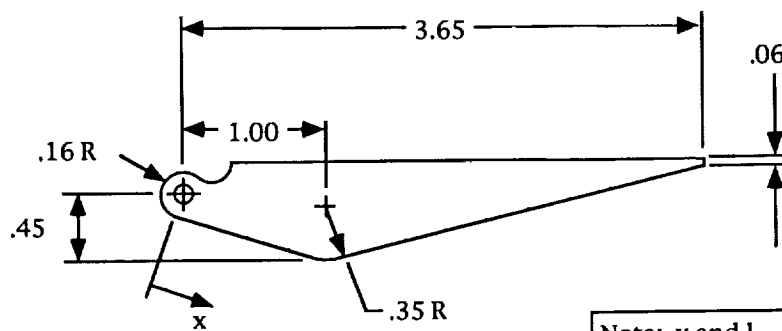
L-93-45

(c) $\delta_v = 105^\circ$, maximum area configuration, forward quarter view.

Figure 4. Concluded.



Minimum area flap
 $l_{uf} = 4.34$ in.

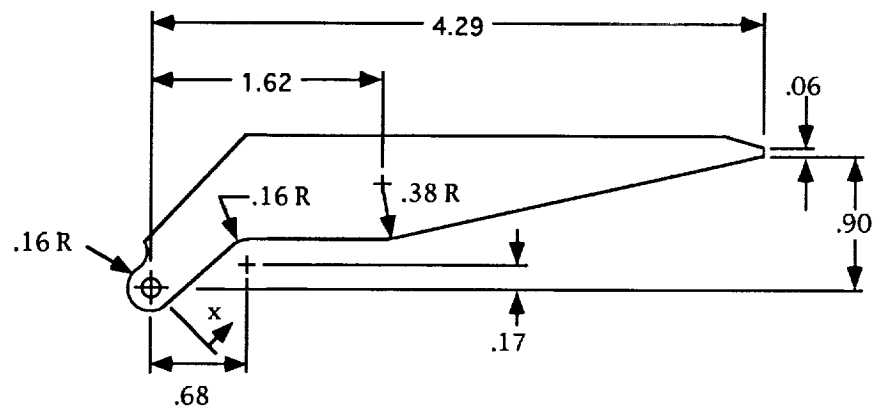


Maximum area flap
 $l_{uf} = 3.91$ in.

Note: x and l_{uf} measured along flap internal surface

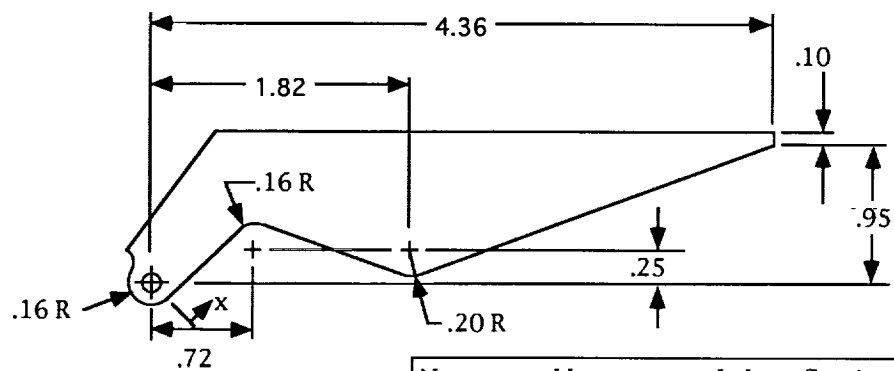
(a) Unvectored upper flaps. $\delta_v = 0^\circ$.

Figure 5. Sketches showing geometry of upper and lower rotating flaps. All linear dimensions are in inches unless otherwise noted.



Maximum area flap

$$l_{uf} = 4.40 \text{ in.}$$



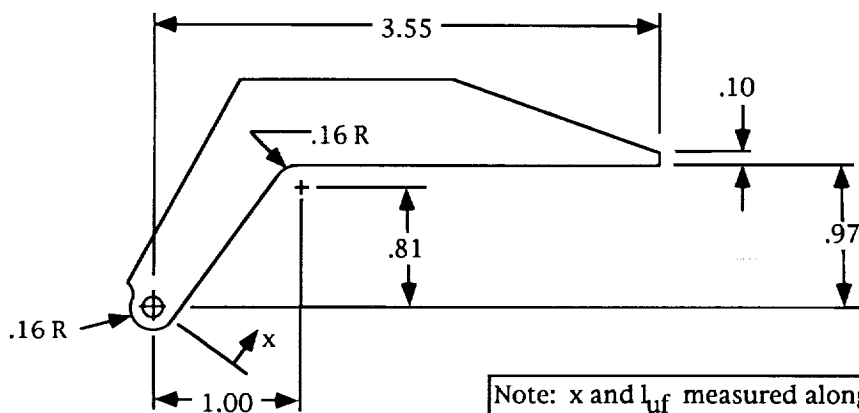
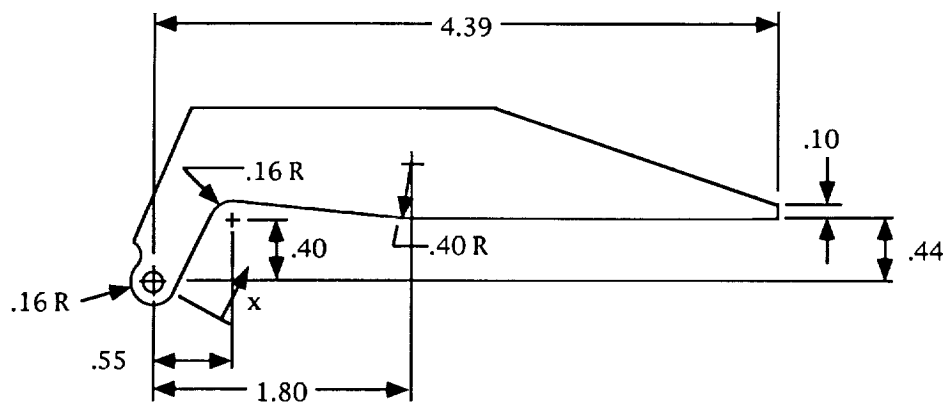
Minimum area flap

$$l_{uf} = 4.67 \text{ in.}$$

Note: x and l_{uf} measured along flap internal surface

(b) Vectored upper flaps. $\delta_v = 60^\circ$.

Figure 5. Continued.

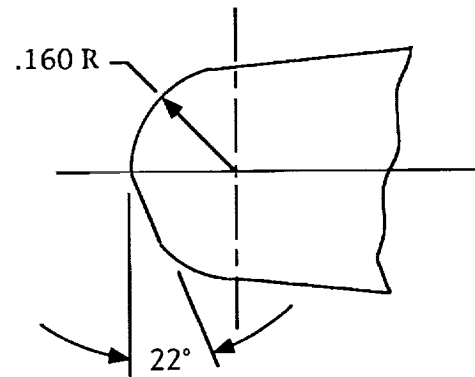


(c) Vectored upper flaps. $\delta_v = 105^\circ$.

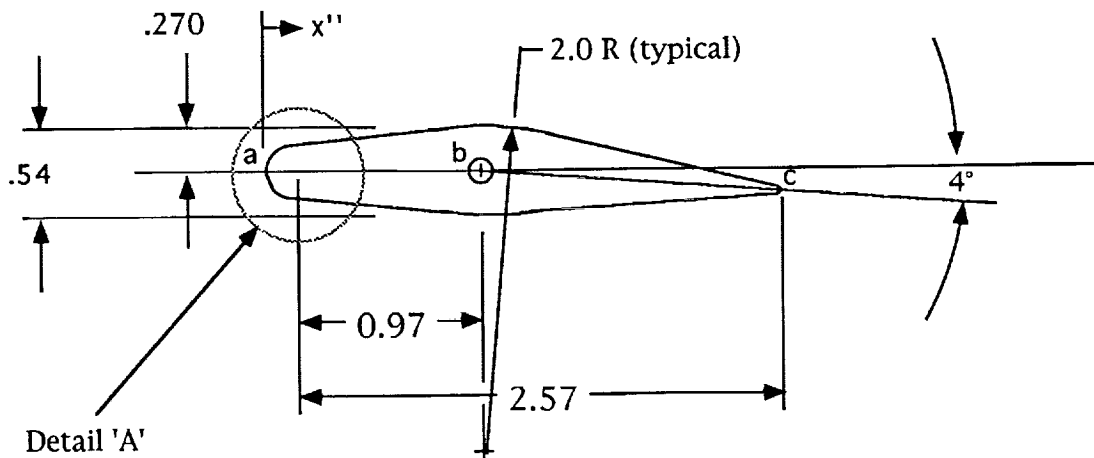
Figure 5. Continued.

Note: The x'' axis follows points a, b, and c.

$l_{lrf} = 3.18$ represents sum of distances a to b and b to c.



Detail 'A'
Scale 4:1



(d) Lower rotating flap.

Figure 5. Concluded.

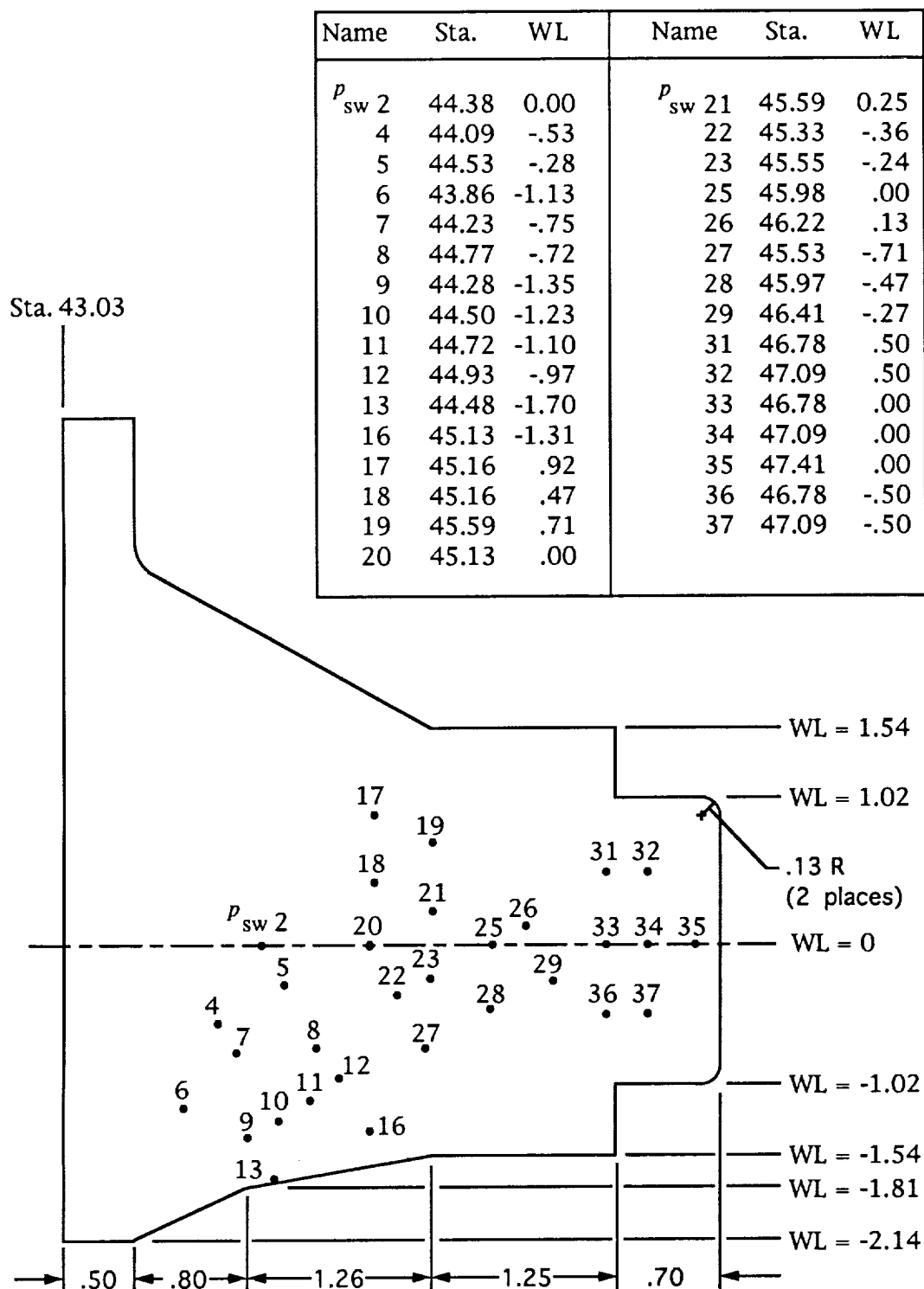


Figure 6. Sidewall dimensions and pressure orifice locations on right sidewall. All linear dimensions are in inches.

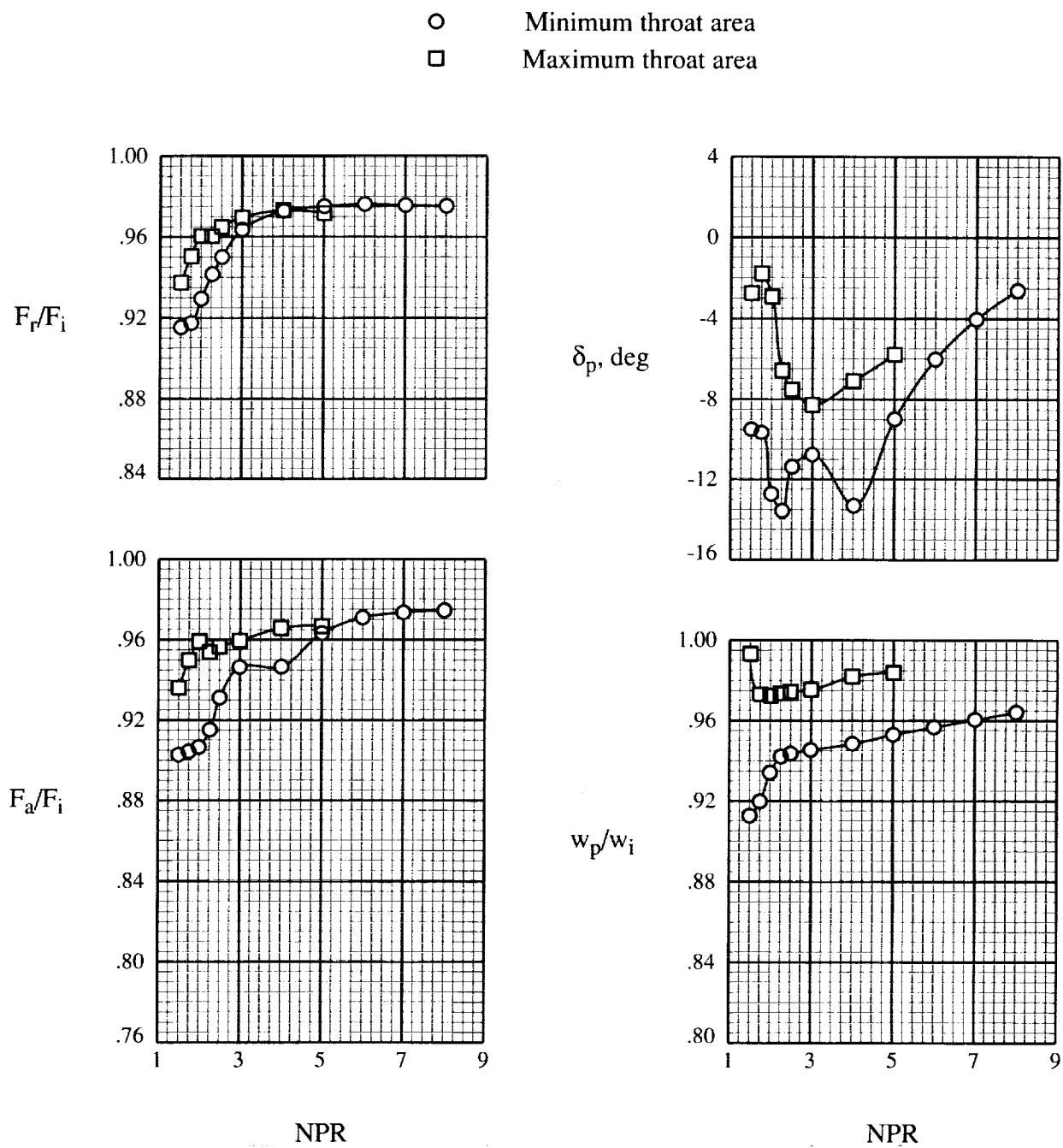


Figure 7. Resultant thrust ratio, thrust-vector angle, axial thrust ratio, and discharge coefficient as functions of nozzle pressure ratio. $\delta_v = 0^\circ$.

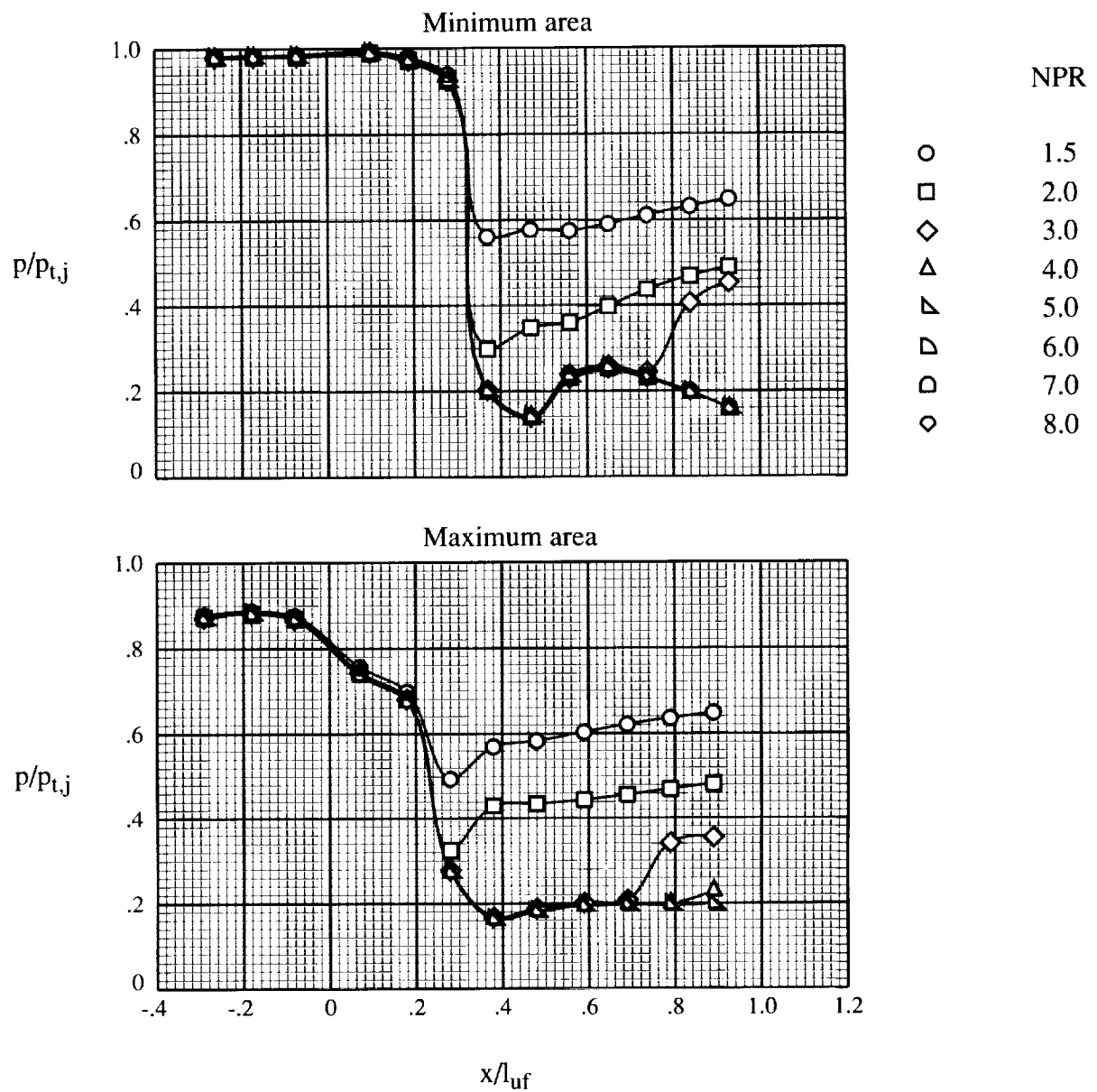


Figure 8. Effect of nozzle pressure ratio on static-pressure distribution of upper flap centerline. $\delta_v = 0^\circ$.

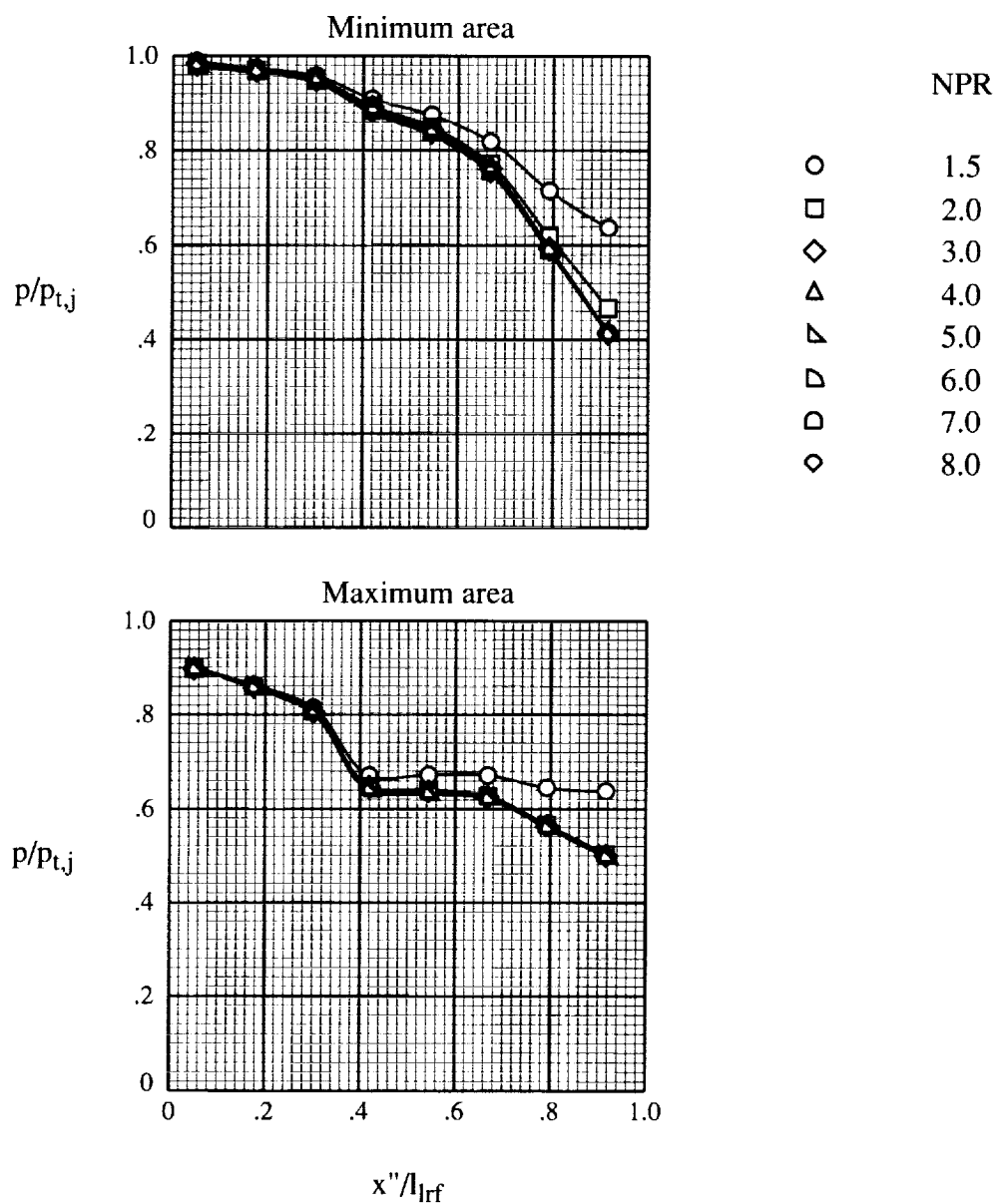


Figure 9. Internal static-pressure distribution along lower rotating flap top surface centerline. $\delta_v = 0^\circ$.



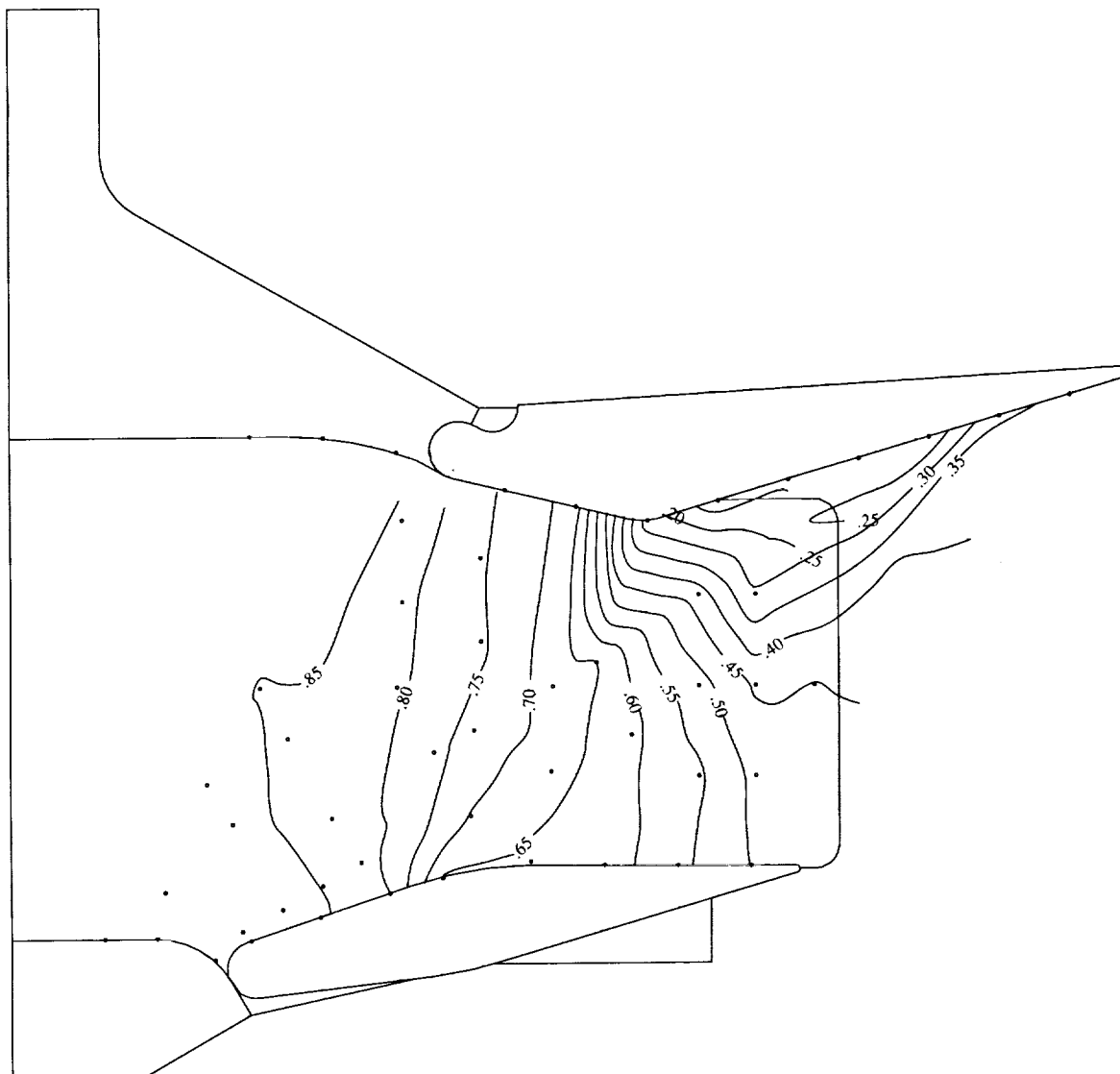
(a) Min 0° configuration. NPR = 3.0.

Figure 10. Sidewall contours of ratio of internal static pressure to jet total pressure.



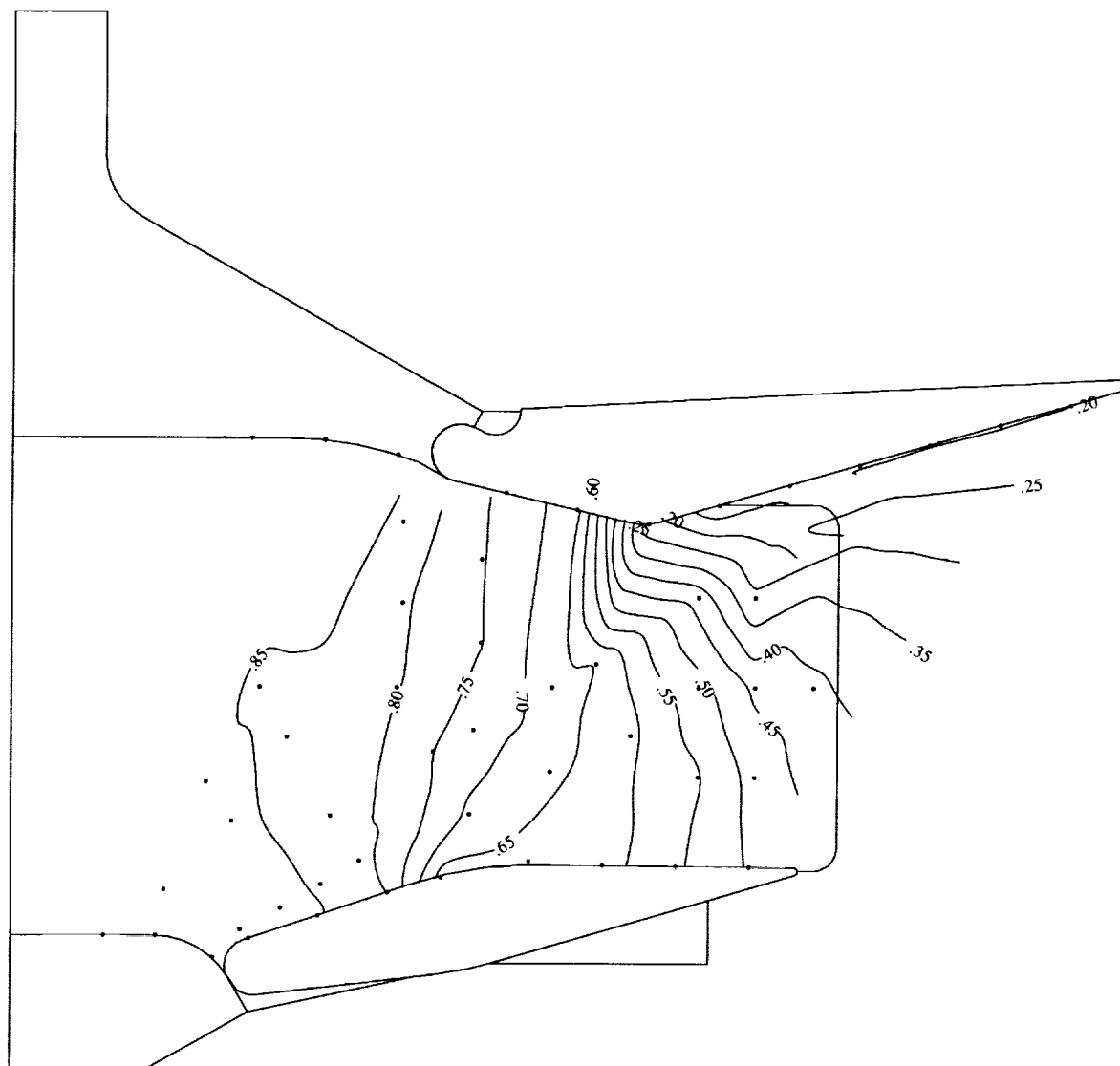
(b) Min 0° configuration. NPR = 7.0.

Figure 10. Continued.



(c) Max 0° configuration. NPR = 3.0.

Figure 10. Continued.



(d) Max 0° configuration. NPR = 5.0.

Figure 10. Concluded.

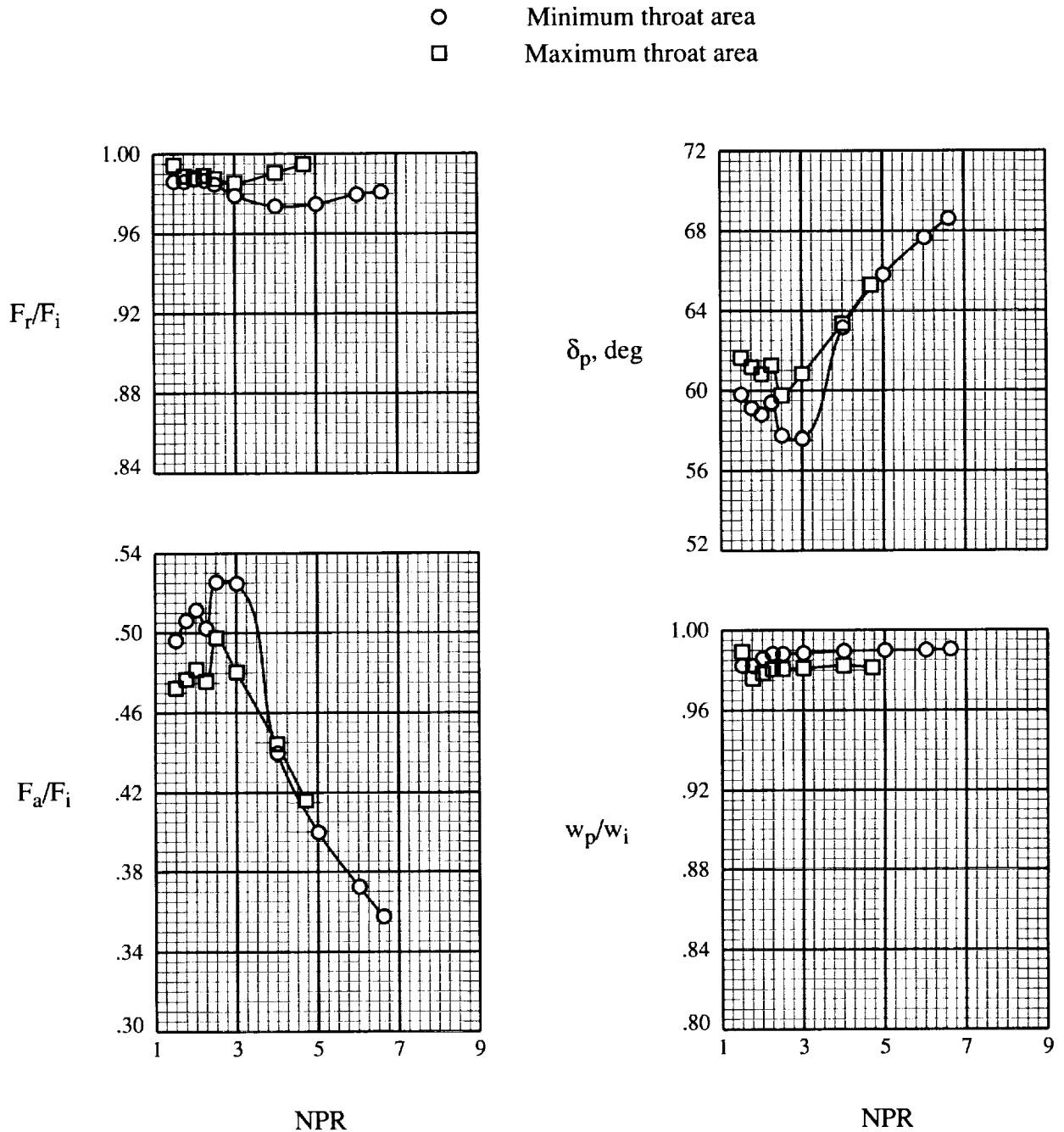


Figure 11. Resultant thrust ratio, thrust-vector angle, axial thrust ratio, and discharge coefficient as functions of nozzle pressure ratio. $\delta_v = 60^\circ$.

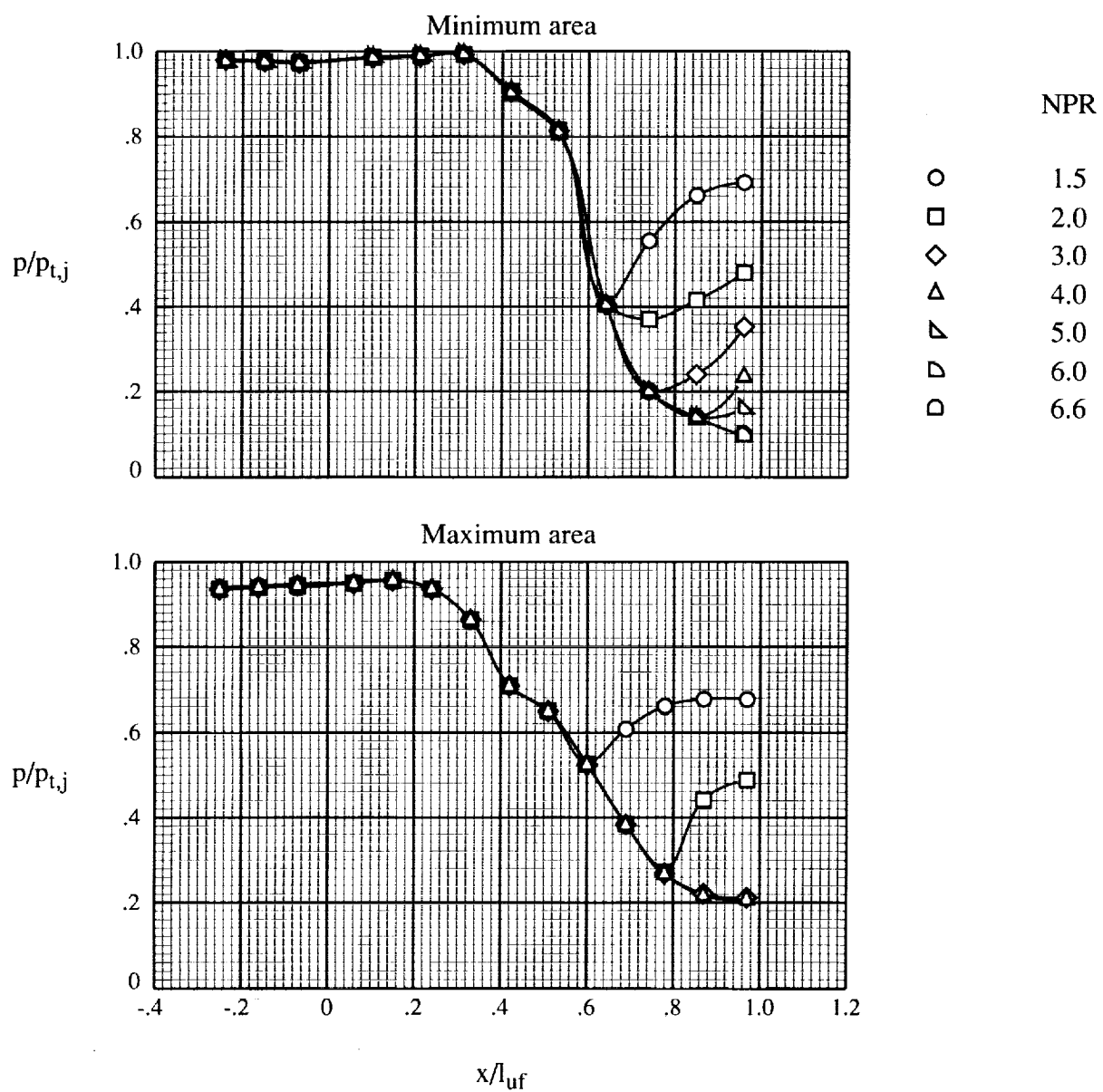


Figure 12. Effect of nozzle pressure ratio on static-pressure distribution of upper flap centerline. $\delta_v = 60^\circ$.

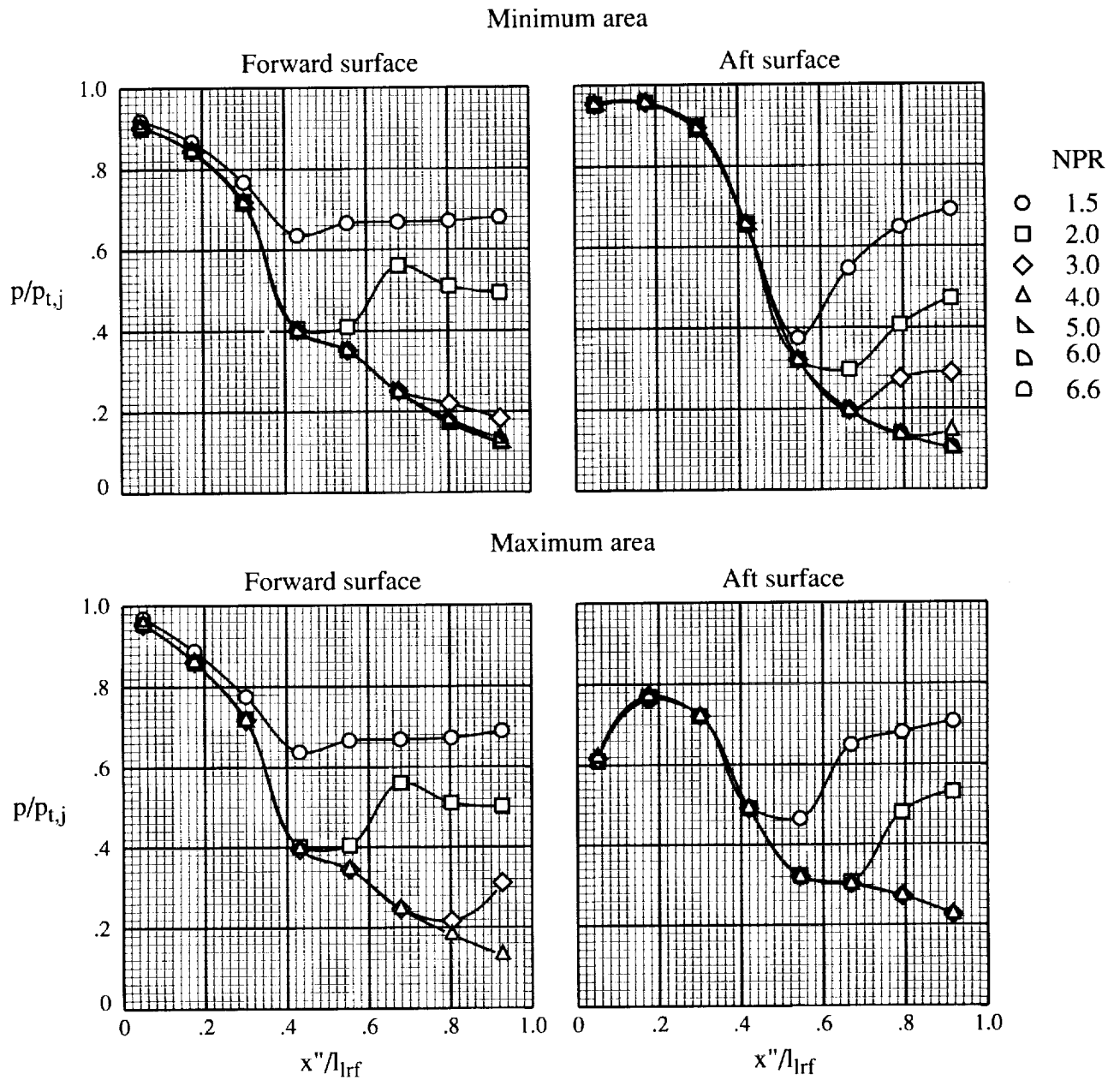
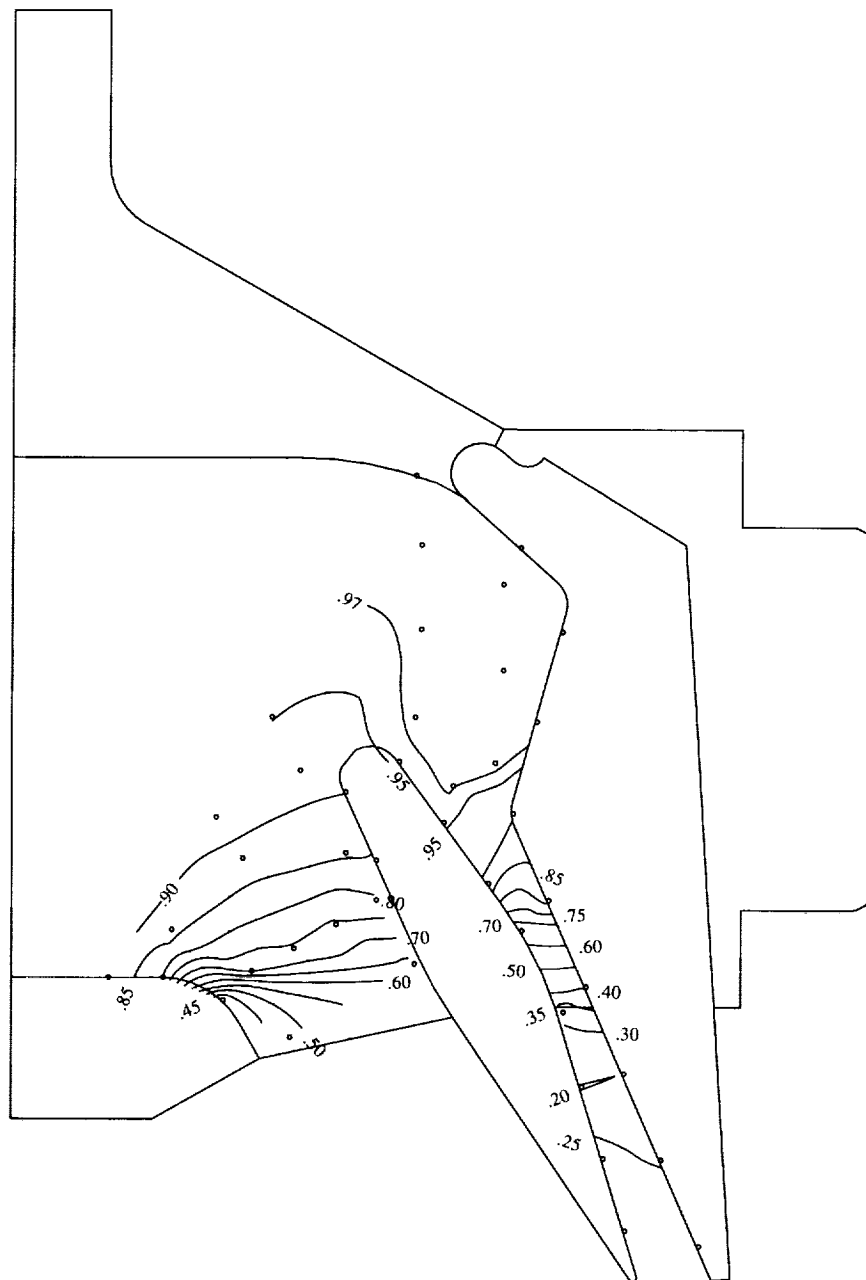
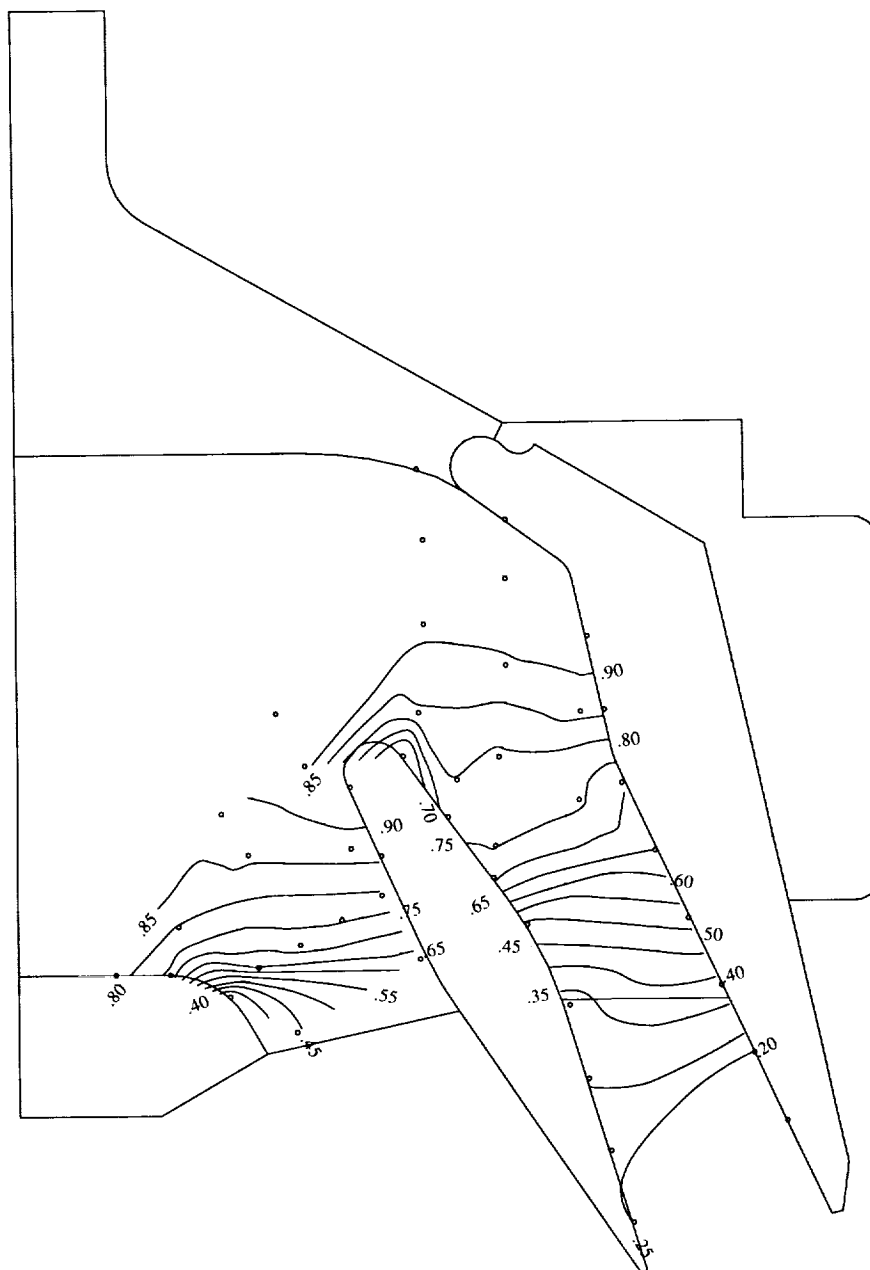


Figure 13. Internal static-pressure distribution along lower rotating flap centerline. $\delta_v = 60^\circ$.



(a) Min 60° configuration. NPR = 3.0.

Figure 14. Sidewall contours of ratio of internal static pressure to jet total pressure.



(b) Max 60° configuration. NPR = 3.0.

Figure 14. Concluded.

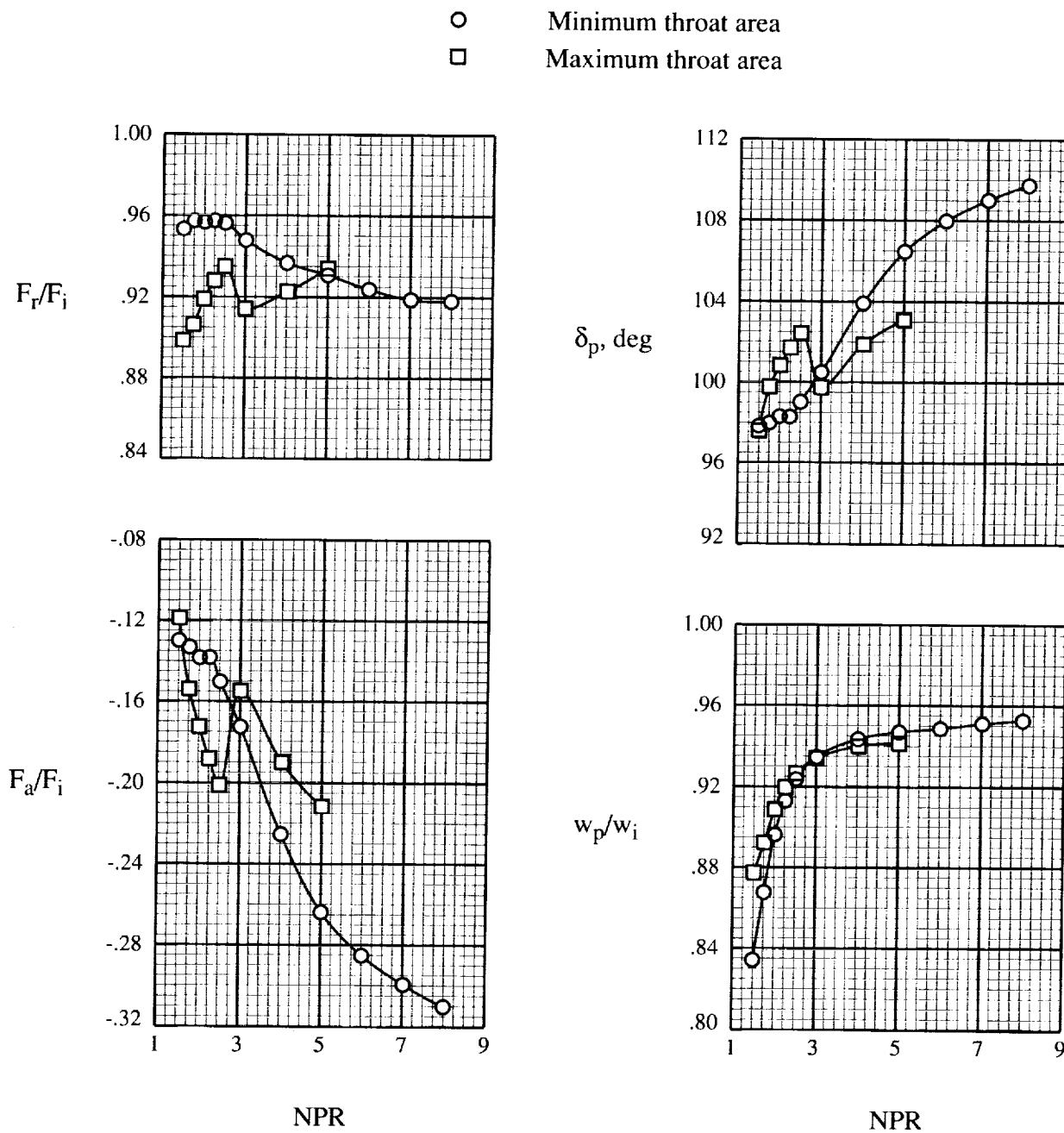


Figure 15. Resultant thrust ratio, thrust-vector angle, axial thrust ratio, and discharge coefficient as functions of nozzle pressure ratio. $\delta_v = 105^\circ$.

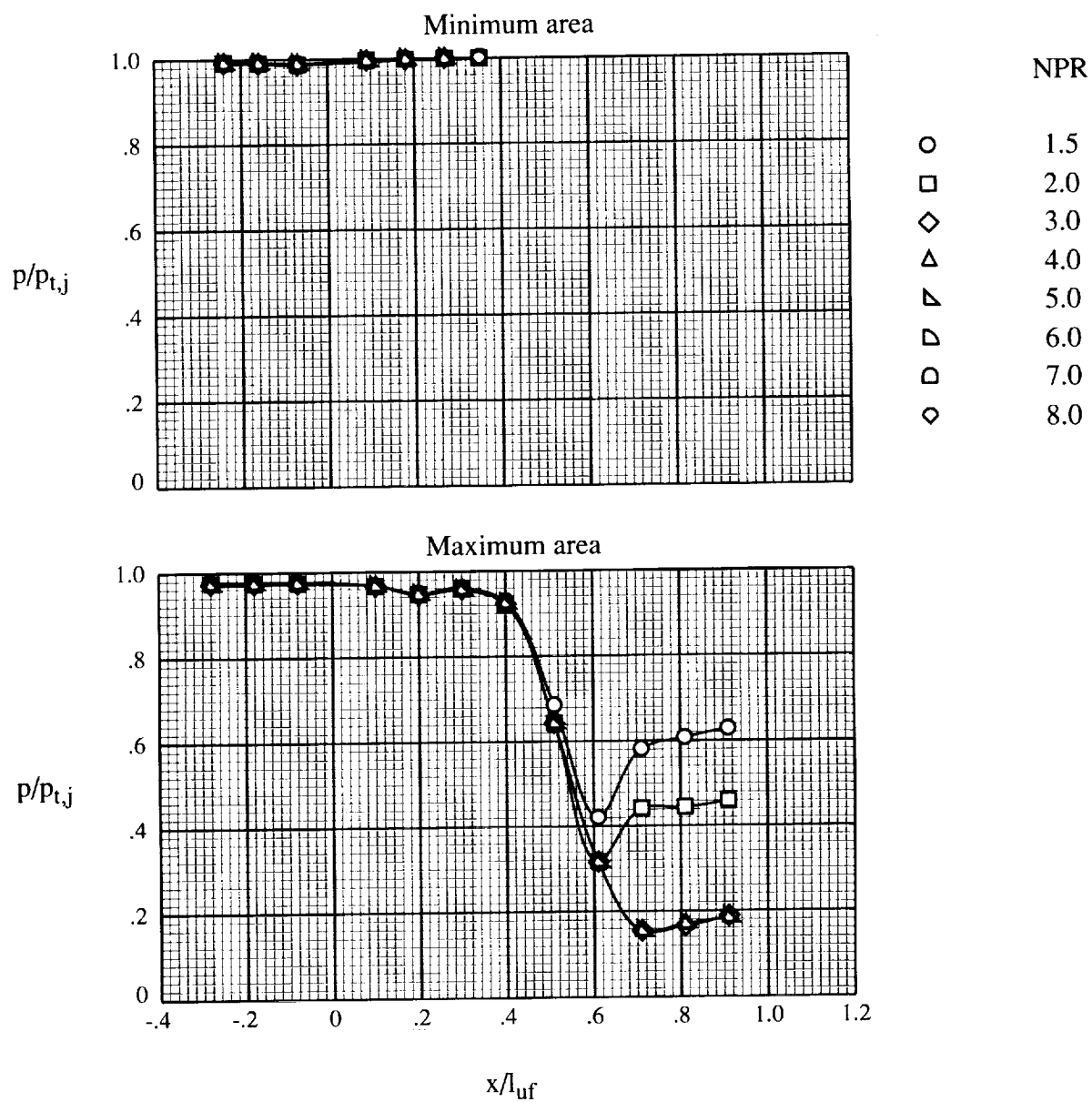


Figure 16. Effect of nozzle pressure ratio on static-pressure distribution of upper flap centerline. $\delta_v = 105^\circ$.

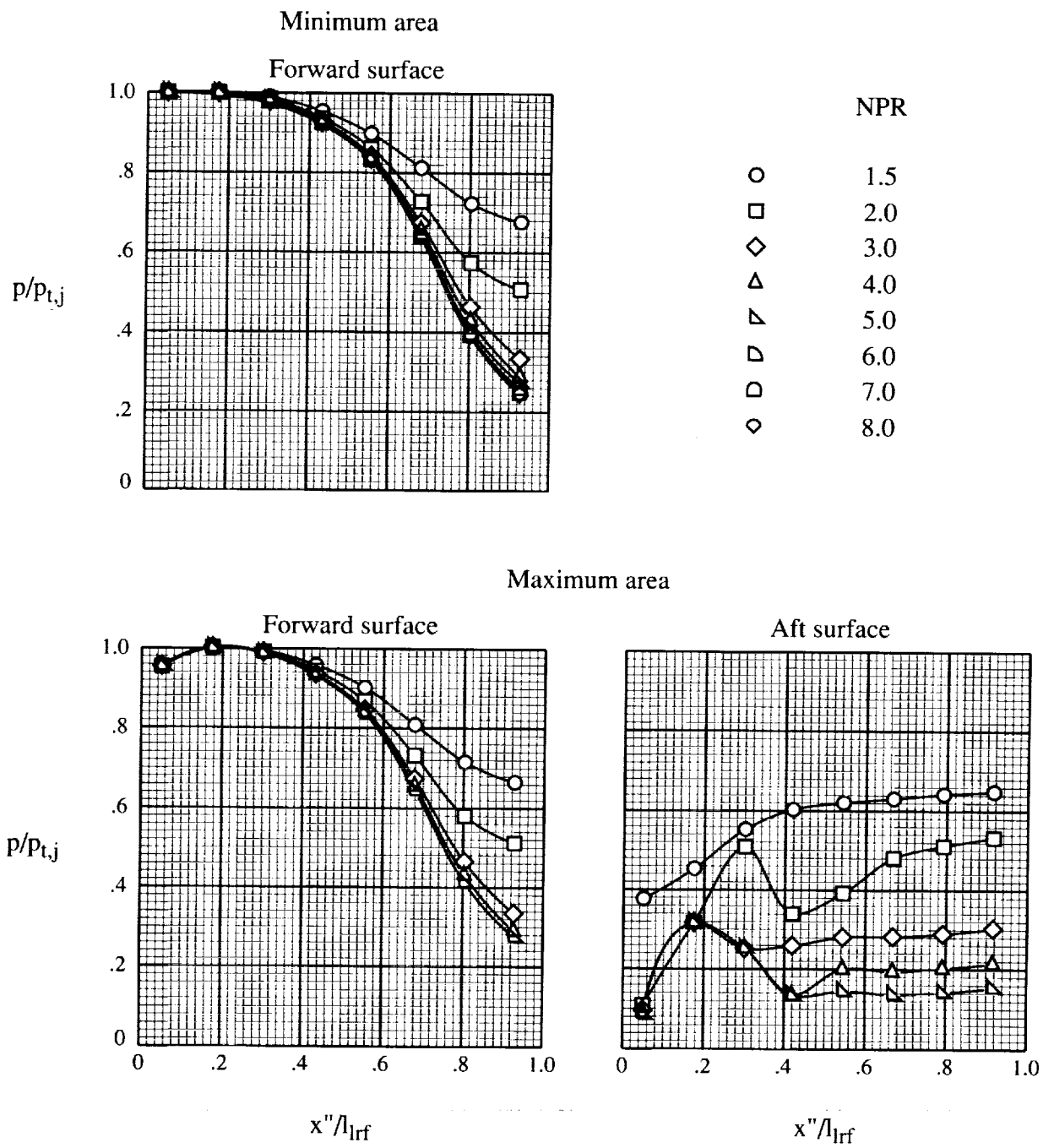
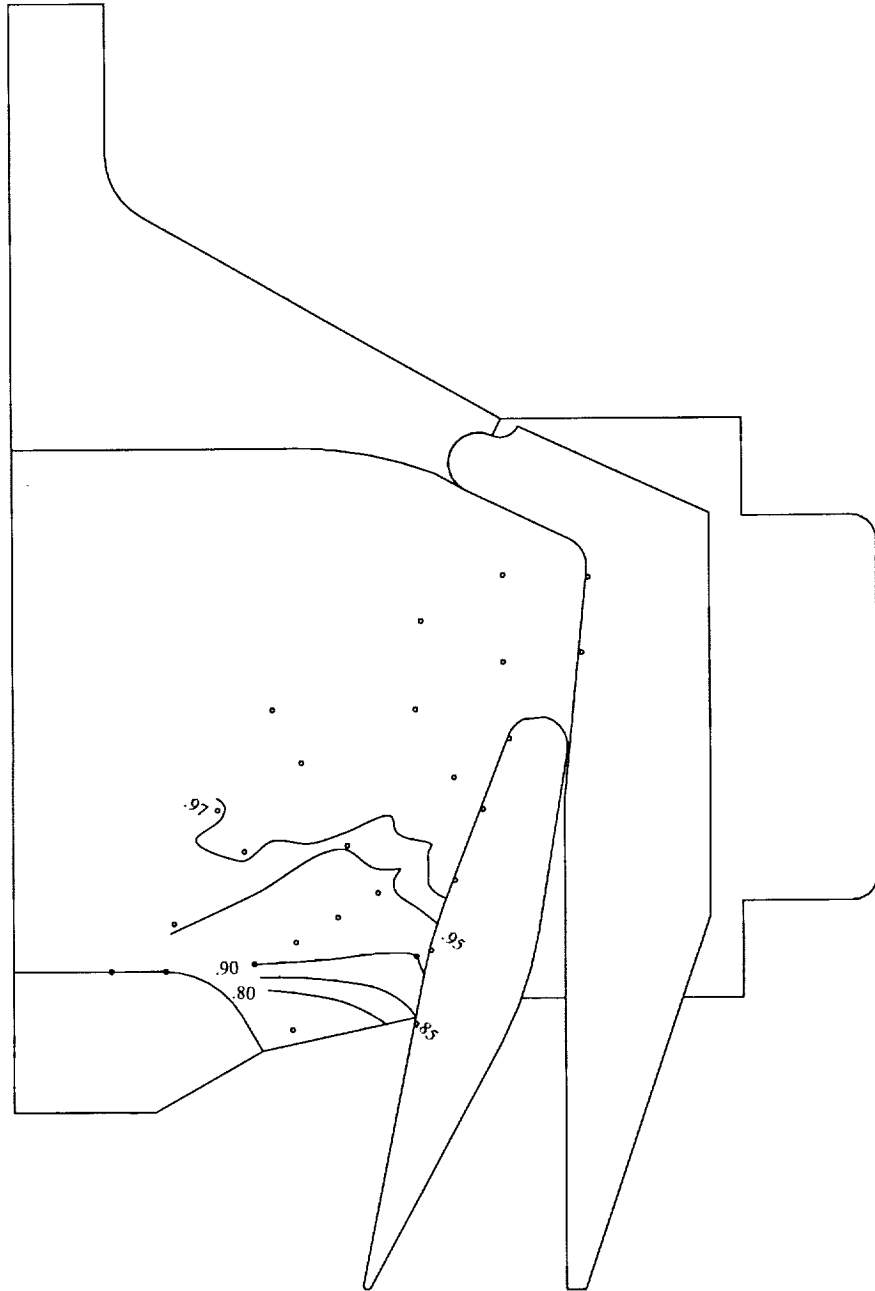
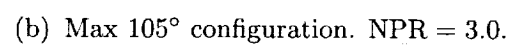


Figure 17. Internal static-pressure distribution along lower rotating flap centerline. $\delta_v = 105^\circ$.



(a) Min 105° configuration. $\text{NPR} = 3.0$.

Figure 18. Sidewall contours of ratio of internal static pressure to jet total pressure.



56

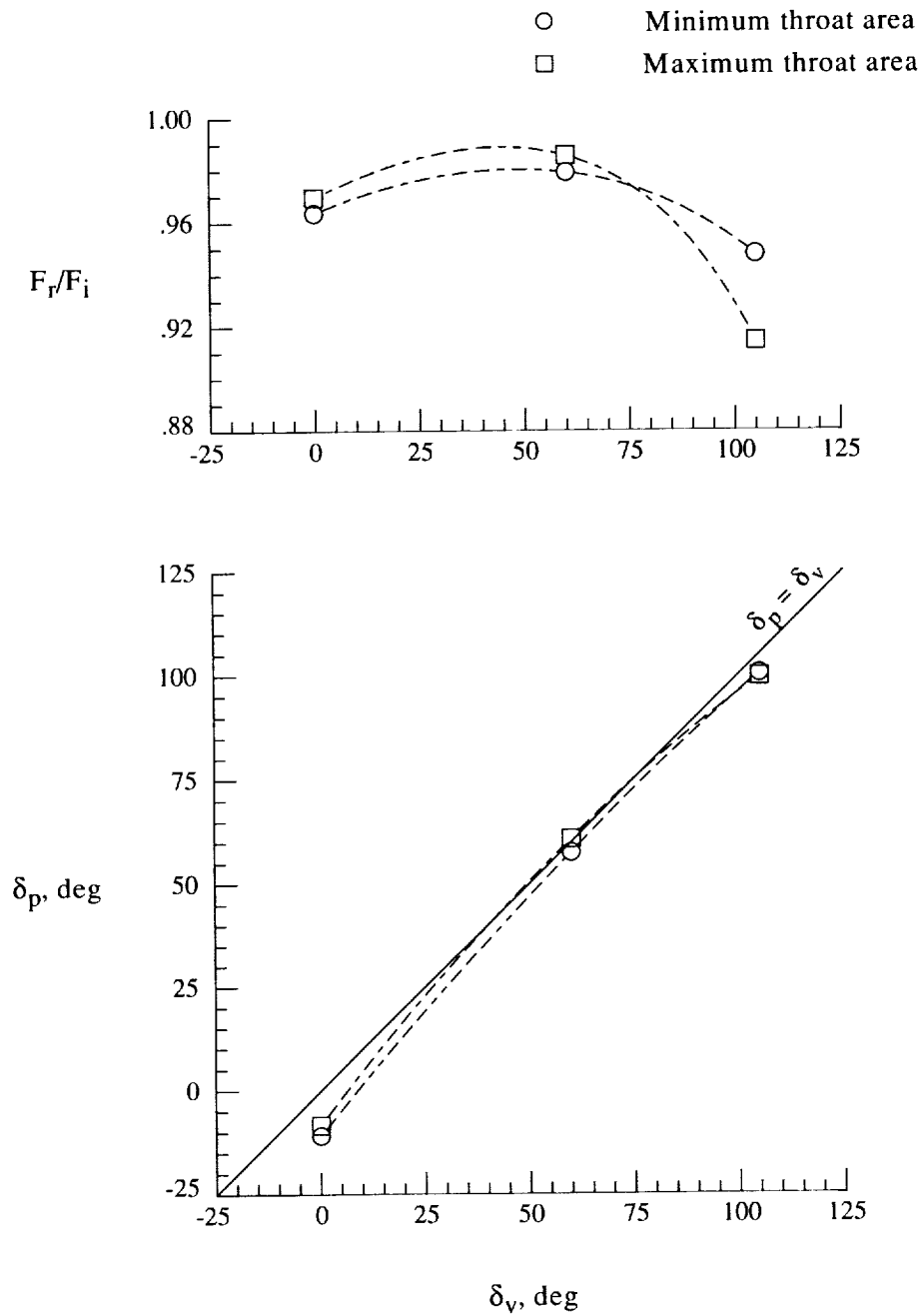


Figure 19. Effect of design vector angle on resultant thrust ratio and thrust-vector angle. NPR = 3.0.

REPORT DOCUMENTATION PAGE			Form Approved OMB No. 0704-0188	
Public reporting burden for this collection of information is estimated to average 1 hour per response, including the time for reviewing instructions, searching existing data sources, gathering and maintaining the data needed, and completing and reviewing the collection of information. Send comments regarding this burden estimate or any other aspect of this collection of information, including suggestions for reducing this burden, to Washington Headquarters Services, Directorate for Information Operations and Reports, 1215 Jefferson Davis Highway, Suite 1204, Arlington, VA 22202-4302, and to the Office of Management and Budget, Paperwork Reduction Project (0704-0188), Washington, DC 20503.				
1. AGENCY USE ONLY (Leave blank)	2. REPORT DATE November 1993	3. REPORT TYPE AND DATES COVERED Technical Paper		
4. TITLE AND SUBTITLE Internal Performance of a Nonaxisymmetric Nozzle With a Rotating Upper Flap and a Center-Pivoted Lower Flap		5. FUNDING NUMBERS WU 505-62-30-01		
6. AUTHOR(S) David J. Wing, Laurence D. Leavitt, and Richard J. Re				
7. PERFORMING ORGANIZATION NAME(S) AND ADDRESS(ES) NASA Langley Research Center Hampton, VA 23681-0001		8. PERFORMING ORGANIZATION REPORT NUMBER L-17235		
9. SPONSORING/MONITORING AGENCY NAME(S) AND ADDRESS(ES) National Aeronautics and Space Administration Washington, DC 20546-0001		10. SPONSORING/MONITORING AGENCY REPORT NUMBER NASA TP-3385		
11. SUPPLEMENTARY NOTES				
12a. DISTRIBUTION/AVAILABILITY STATEMENT Unclassified-Unlimited Subject Category 02		12b. DISTRIBUTION CODE		
13. ABSTRACT (Maximum 200 words) An investigation was conducted at wind-off conditions in the static-test facility of the Langley 16-Foot Transonic Tunnel to determine the internal performance characteristics of a single expansion-ramp nozzle with thrust-vectoring capability to 105°. Thrust vectoring was accomplished by the downward rotation of an upper flap with adaptive capability for internal contouring and a corresponding rotation of a center-pivoted lower flap. The static internal performance of configurations with pitch thrust-vector angles of 0°, 60°, and 105°, each with two throat areas, was investigated. The nozzle pressure ratio was varied from 1.5 to approximately 8.0 (5.0 for the maximum throat area configurations). Results of this study indicated that the nozzle configuration of the present investigation, when vectored, provided excellent flow-turning capability with relatively high levels of internal performance. In all cases, the thrust vector angle was a function of the nozzle pressure ratio. This result is expected because the flow is bounded by a single expansion surface on both vectored- and unvectored-nozzle geometries.				
14. SUBJECT TERMS Nozzles; Thrust vectoring; Single expansion-ramp nozzle (SERN); Short takeoff and vertical landing (STOVL)			15. NUMBER OF PAGES 58	
			16. PRICE CODE A04	
17. SECURITY CLASSIFICATION OF REPORT Unclassified	18. SECURITY CLASSIFICATION OF THIS PAGE Unclassified	19. SECURITY CLASSIFICATION OF ABSTRACT	20. LIMITATION OF ABSTRACT	